JOURNAL OF AIRCRAFT
Vol. 47, No. 1, January–February 2010

# Small Rotor Design Optimization Using Blade Element Momentum Theory and Hover Tests

Felipe Bohorquez,* Darryll Pines,† and Paul D. Samuel‡
*University of Maryland, College Park, Maryland 20742*

DOI: 10.2514/1.45301

**The current investigation focuses on the development of a low-cost computational methodology to design and optimize hovering rotors for small-scale vehicles using circular arc airfoils. Rotors for vehicles having a representative *Re* between 5000 and 60,000 were considered. A detailed experimental study of rectangular and tapered blades generated the data necessary to identify main performance trends and the effect of planform modifications. A blade element momentum theory model coupled with a table lookup scheme was implemented. The database was interpolated along three dimensions (*Re*, camber, and angle of attack) to obtain the local aerodynamic coefficients used in the calculation of the nonlinear inflow distribution along the blade span. Two methodologies were used in the calculation of the database. First, a purely numerical approach using the two-dimensional flow solver INS2D was evaluated. Second, a reverse method that used the experimental rotor data to refine the original previously generated database was investigated. Validation showed that the model predictive capabilities improved with the empirical corrections. An optimization algorithm was implemented to perform a grid search using power loading as the hover efficiency metric. The methodology proposed is able to optimize blade geometry and operating conditions following imposed constraints within a defined design space.**

## Nomenclature

| | | |
|---|---|---|
| $A$ | = | rotor disk area |
| $C_d$ | = | section drag coefficient |
| $C_{d\,\min}$ | = | minimum drag coefficient |
| $C_l$ | = | section lift coefficient |
| $C_m$ | = | section moment coefficient |
| $C_{l\,\max}$ | = | maximum lift coefficient |
| $C_P$ | = | rotor power coefficient, $P/\rho A(\Omega R)^3$ |
| $C_T$ | = | rotor thrust coefficient, $T/\rho A(\Omega R)^2$ |
| $c$ | = | blade chord |
| $M$ | = | Mach number |
| $Nb$ | = | number of blades |
| $P$ | = | rotor power |
| $R$ | = | blade radius |
| $Re$ | = | Reynolds number based on chord |
| $r$ | = | radial distance |
| $T$ | = | rotor thrust |
| $\alpha$ | = | angle of attack |
| $\rho$ | = | density of air |
| $\sigma$ | = | rotor solidity, $Nbc/\pi R$ |
| $\Omega$ | = | rotational frequency of rotor |

## I. Introduction

IN 1996, the concept of micro air vehicles (MAVs) was first introduced to the scientific community by the Defense Advanced Research Projects Agency (DARPA). The objective of the MAV program was to develop and test mission-capable prototypes to be used in civilian or military surveillance and reconnaissance applications. The program pushed the boundaries of existing technologies in fields as diverse as aerodynamics, propulsion, power generation, electronics, and design. Results were encouraging but not completely satisfactory. After four years of research, the vehicles developed were far from achieving the 1 h endurance sought by DARPA. Development continued after the program ended and only a few designs reached the production line.

Fixed-wing vehicles such as Aerovironment's Black Widow and Lockheed Martin's Microstar have been relatively successful, having sophisticated navigation and control systems and endurance times between 20 and 30 min. However, fixed-wing vehicles are limited to loiter above the target at high altitudes, preventing their use in urban and indoor scenarios. For these types of missions, vertical takeoff and landing (VTOL) vehicles are required. A stealthy hovering MAV can fly indoors without being detected and is capable of "perch and stare," providing tactical reconnaissance and surveillance for extended time. Existing VTOL MAVs are generally heavier, larger, and have shorter endurance than fixed-wing vehicles. Designs such as the University of Maryland's Giant or SRI's flapping concept, the MENTOR [1,2], have not yet been able to remain aloft for more than 10 min and have very limited maneuverability. Larger vehicles such as the ISTAR (Allied Aerospace [3]) can remain aloft for considerably longer times, but their greater weight and size excludes them from the MAV category.

In the broad range of possible applications, there is a niche for stealthy VTOL MAVs. However, the technical problems that need to be overcome to achieve better endurance within the size and weight constraints have posed significant challenges for engineers. One of the main issues that limits the vehicle's hover performance is the degraded aerodynamic characteristics of airfoils and rotors at small scale. The design requirements for MAVs established tight size constraints, requiring the vehicles to be an order-of-magnitude smaller than previously developed systems, requiring them to operate at low-*Re* aerodynamic flow conditions. Whereas full-scale helicopters can have figures of merit up to 0.8, nonoptimized small-scale rotor efficiencies range from 0.3 up to 0.6 [4–6]. Historically, systems operating below a *Re* of 1 million were considered to be in the lower Reynolds number regime. However, since the introduction of unmanned aerial vehicles (UAVs), the term "low-Reynolds-number design" is loosely used for vehicles with many different and varied characteristics. Within the MAV vehicle class, a large variation in scale and operating conditions occurs. Small commercially available helicopters have representative chord-based

Received 5 May 2009; revision received 28 July 2009; accepted for publication 29 July 2009. 

*Graduate Research Assistant, Smart Structures Laboratory, Alfred Gessow Rotorcraft Center, Department of Aerospace Engineering.

†Professor of Aerospace Engineering, Smart Structures Laboratory, Alfred Gessow Rotorcraft Center, Department of Aerospace Engineering. Member AIAA.

‡Research Associate, Smart Structures Laboratory, Alfred Gessow Rotorcraft Center, Department of Aerospace Engineering.

*Re* on the order of 100,000, whereas research prototypes like the Giant and MICOR [2,7], developed at the University of Maryland, cover the range between 30,000 and 60,000, having rotor diameters ranging from 18 to 23 cm and a weigh of 200–400 g. Next generation vehicles that are currently under development are 1-order-of-magnitude lighter than MAVs, having a mass of about 15 g and a maximum dimension no larger than 7.5 cm. This emerging new class of vehicles, known as nano air vehicles (NAVs), operate in the lower range between 5,000 and 20,000 *Re*.

Over the Reynolds number range under consideration ($5 < Re < 60$ k), distinct aerodynamic regimes have been identified, as reported by Carmichael in his well known low-*Re* airfoil survey [8]. This dependence of an airfoil's sectional characteristics on *Re* makes it a challenge to design or choose a unique airfoil with good aerodynamic performance over the entire MAV–NAV design space. Similarly, available power plants for MAV/NAV implementation, typically electric motors, achieve their maximum efficiencies at very distinct torque and rotational speeds depending on their power rating, size, and technology. The wide array of possible vehicle configurations, operating conditions, and mission profiles requires the vehicle's complete propulsion system to be designed as a whole, properly matching the rotor, motor, and transmission to maximize the overall vehicle performance. Finding an optimal configuration requires an intensive iterative process, where it is key to have short design cycles. For the aerodynamic calculations, current state-of-the-art computational methods such as 3-D computational fluid dynamics (CFD) and vortex modeling, which are commonly used in full-scale design, are still not mature enough to be efficiently used in small-scale applications. These methods require extensive experimental validation and vast computational resources, which lengthen the design cycles, rendering them impractical for the limited resources and fast-paced design procedure sought.

This paper proposes a low computational cost approach to systematically design and optimize MAV–NAV propulsion systems within a defined design space using power loading as the efficiency metric. A blade element momentum theory (BEMT) based rotor model coupled with a table lookup scheme is used in an optimization algorithm to determine the optimal blade and rotor configuration that meets the constraints imposed for a particular design. The airfoil database is restricted to a family of circular arc airfoils and is calculated using a two-dimensional CFD solver. The CFD-generated database was empirically corrected using rotor tests to improve the predictive capabilities of the model. The approach was validated by performing detailed hover rotor testing of various rotor configurations.

## II. Low-*Re* Airfoil Aerodynamics

As Reynolds number is reduced, viscous forces become dominant, resulting in a complex boundary-layer behavior. Phenomena such as transition, separation, and reattachment can occur within a short chordwise distance, having a large effect on pressure distribution and airfoil performance. For low-*Re* applications, as for full-scale designs, minimization of the airfoil's shear drag is desired. This can be achieved by minimizing the regions along the airfoil that have separated flow. Hence, at low *Re*, a turbulent boundary layer is generally preferred due to its better stability characteristics. In his 1981 survey, Carmichael [8] divided the Reynolds number realm into 12 segments covering 10 orders of magnitude. In the Reynolds number range of interest for MAVs and NAVs, three of these regimes are covered.

The first regime starts at a *Re* of 1000 and covers 1 order of magnitude, reaching a *Re* of 10,000. This range is relevant for the smaller-size vehicles such as NAVs. The flow in this regime is characterized by being laminar with a tendency to separate before undergoing transition. The research performed on the Mesicopter [9] is a good example of a design in this regime. Computational results suggest that airfoil design, and in particular camber distribution, is an important factor that affects airfoil performance.

The second regime covers Reynolds numbers between 10,000 and 30,000. Here, the flow exhibits a similar behavior to that of the immediately lower regime, being laminar with a tendency to separate before transitioning into turbulent. Limited research has been performed in this regime, and it is not clear if reattachment can be promoted by the use of boundary-layer trips.

The third regime covers the Reynolds numbers between 30,000 and 70,000. This regime is where most of the fixed-wing MAVs and the outer sections of MAV rotors operate. Flow in this regime is characterized by the occurrence of laminar separation bubbles that introduce hysteresis in the experimental measurements. Below a Reynolds number of about 50,000 the chordwise distance is generally not sufficient for reattachment to occur; however, experiments have shown that the use of boundary-layer trips or turbulators to reduce the critical Reynolds number (Reynolds number at which transition occurs) has been successful near the upper bound of this range.

Finally, the regime that covers Reynolds numbers between 70,000 and 200,000 is characterized by the ease of laminar to turbulent flow transition without separation. Turbulators can still be useful to reduce the size of the separation bubbles at the lower bound of the interval. Most of the low-*Re* experimental research falls into this regime, which is typical of fixed-wing radio control models and UAVs larger than MAVs.

The body of aerodynamic research in the literature suggests that massive flow separation and laminar separation bubbles are in large part responsible for the poor aerodynamic performance of conventional airfoils at low *Re*. A good airfoil design should reduce the occurrence of flow separation and bubble formation, or should have aerodynamic characteristics relatively independent of these boundary-layer phenomena. This type of behavior was first identified by Schmitz in the 1940s [10] when comparing the behavior of streamlined airfoils and thin plates over a Reynolds number range of 42,000–420,000 using a low-turbulence wind tunnel.

The results reported by Schmitz [10] made the positive aero dynamic characteristics of thin curved plates at low *Re* evident. He studied the Go417a airfoil, a curved plate with 6% maximum camber at 40% of the chord with a uniform thickness ratio (TR) of 2.9%. Figures 1a and 1b are plotted using Schmitz's data and show how a representative streamlined airfoil, like the N60, suffers from a large drop in maximum lift and an increase in minimum drag coefficients as *Re* is reduced below 100,000. The thin curved plate airfoil shows a very different behavior, being able to maintain almost constant values of lift and drag coefficients over the Reynolds number range covered.

Laitone [11], following on Schmitz's results [10], investigated the superior aerodynamic performance of sharp-nosed thin circular arc plates over round-nosed streamlined airfoils at low *Re*. His results [11] showed how the small nose radii of thin plates continually shed small vortices that rolled along the upper surface, preventing flow separation over a range of angles of attack.

These findings complement Schmitz's results [10], that attributed the good airfoil performance to the large adverse pressure gradients produced by the relatively sharp leading edges. Schmitz suggested that the large gradients work as boundary-layer trips that induce early transition, making the upper surface boundary layer more resilient to disturbances.

Schmitz [10] and Laitone's [11] research focused on specific thin cambered airfoils (Go417a and 5% camber circular arc, respec tively), providing just a few data points. Over the last decade, thanks to the renewed interest in low-*Re* aerodynamics, additional research on the aerodynamics of cambered plates and circular arcs has been published; nevertheless, large experimental gaps are still present in the available experimental data.

Thin cambered plates, particularly circular arcs, may not be an optimum choice in terms of aerodynamic performance; however, they possess a series of attributes that can make them a good choice for small-scale vehicle implementation. In addition to their satis factory aerodynamic characteristics, the manufacturing of curved plates is generally simple due to their uniform thickness. This is particularly true when considering circular arcs, which can be easily molded from cylinders and cones without the need to manufacture intricate molds. Because of their ease of manufacturing, geometric simplicity, and performance benefits, the research presented in this

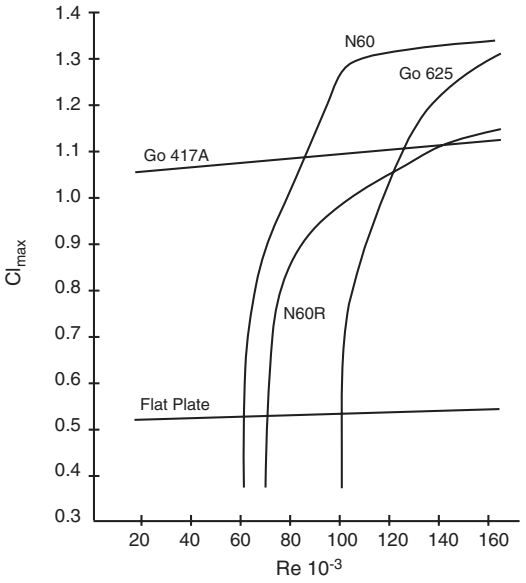


**a) Reynolds number vs maximum lift coefficient for airfoils studied by Schmitz [10]**

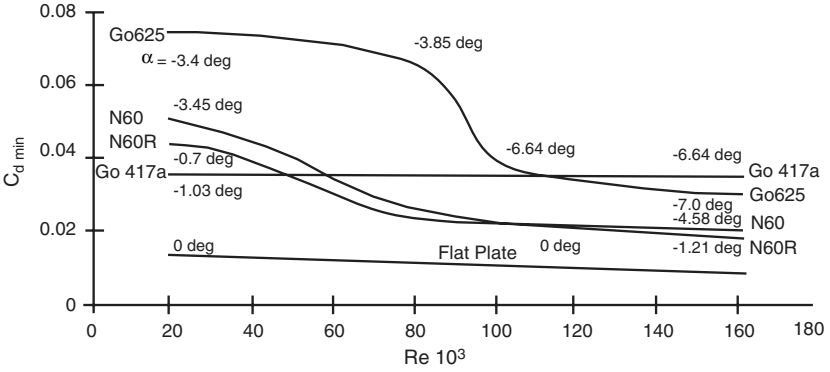


**b) Reynolds number vs minimum drag coefficient for airfoils studied by Schmitz [10]**

**Fig. 1 Effect of *Re* on maximum lift coefficient and minimum drag for the airfoils studied by Schmitz. Plots generated from data presented in [10].**

paper focuses on a specific family of circular arcs previously used by Mueller in the wind-tunnel tests of [12].

The geometries defined have elliptical leading edges and sharp trailing edges that cover varying chordwise distances that are a function of the airfoil's thickness and chord. This results in airfoils with leading edges that extend for a larger chord fraction as thickness ratio increases. Figure 2 shows the proportions used.

## III. Blade Geometry Parameterization

Conventional rotor blades generally use a combination of taper and twist to achieve higher levels of hover performance. The spanwise distributions of these parameters are not coupled to each other or to the airfoils' shapes of the blades. When using circular arcs as airfoils, couplings in the geometry are introduced simply by removing material from a baseline rectangular planform, simultaneously modifying the following rotor and airfoil parameters: 1) taper, 2) solidity, 3) twist distribution, 4) airfoil camber, and 5) airfoil thickness ratio.

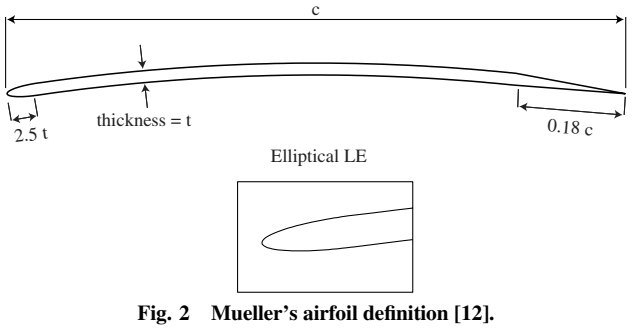


**Fig. 2 Mueller's airfoil definition [12].**

Couplings between camber and taper are a function of the airfoil shape and the local chord: the higher the chord reduction, the lower the resulting camber in the remaining blade section. Similarly, couplings between twist and taper are dependent on the local chord, the local camber, and the geometry of the tapering. This is illustrated in Fig. 3 which shows two blades with identical taper ratio but different geometries. Figure 3a shows a radially symmetric taper that results in no added twist, whereas Fig. 3b shows a fully asymmetric taper that introduces negative twist. Couplings between airfoil camber, twist, and taper are obviously not present when flat plate airfoils are used. In that case, the tapering only affects the airfoil thickness ratio.

An additional level of geometric tailoring is added when the baseline rectangular blade incorporates twist or a nonuniform camber distribution before any planform modification. In that case, the effects of the material removal from the baseline blade are superimposed, giving more control over the final blade geometry.

The use of the previous methodology is particularly convenient for systematic experimentation and mathematical modeling of the blade geometry. Because all generated airfoil shapes are circular arcs, it is possible to derive the geometric couplings between planform and blade parameters for a family of circular arc airfoils.

### A. Blade Geometry Definition

Blade and airfoil parameters determine in large part the efficiency of a hovering rotor. Taper and twist are generally used to optimize the

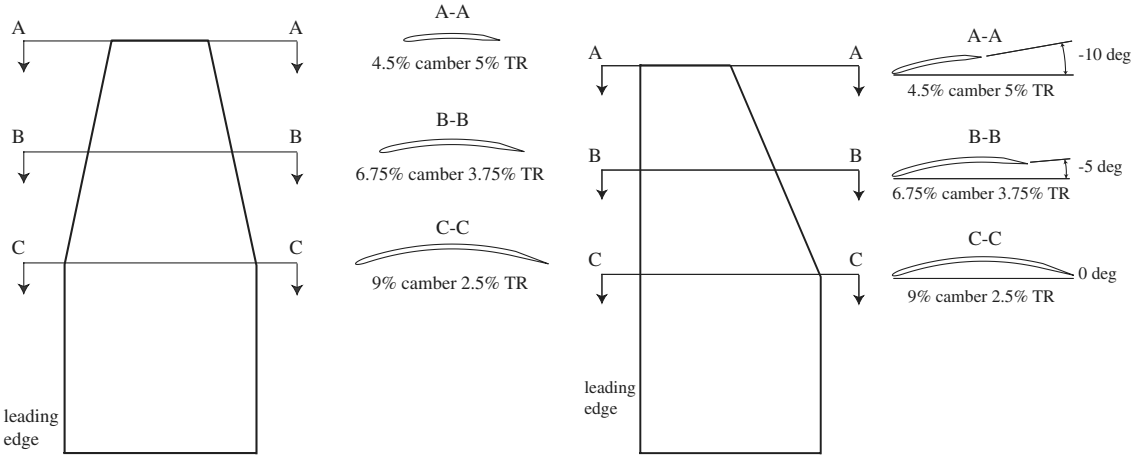


**a) Symmetric** **b) Asymmetric**

**Fig. 3 Geometric effects of symmetric and asymmetric 2:1 linear taper on blade with baseline 9% circular arc airfoil.**

rotor performance by reducing the induced and profile power requirements. Taper reduces the local solidity of the blades and, consequently, the inflow, whereas twist has a direct effect on the local lift and drag coefficients at which the blade sections operate. With the right combination of twist and taper, a more uniform inflow and higher lift-to-drag ratios can be achieved along the blade span.

In this investigation, blade geometry is defined by two sets of linearly interpolated control points: one set delineates the planform and a second specifies the twist distribution of the baseline rectangular blade. The spanwise camber distribution of the baseline blade is also a linear distribution between the root and tip camber values. Six control points are used for the planform definition and three more for the twist distribution.

Control points are constrained to define planforms consistent with material removal from a rectangular baseline blade. As illustrated in Fig. 4, points 3 and 4 are constrained to move vertically along the blade tip, whereas points 2 and 5 are can only move horizontally along the baseline leading edge (LE) and trailing edge, respectively. Points 1 and 6 are aligned vertically at the specified root cutout location. The twist distribution shown in Fig. 5 requires three points and adds three more variables to the planform definition: radial location and twist of the intermediate control point, and root twist. The outermost control point is fixed at the tip ($r = 1$) with a zero twist value.

Adding the root and tip cambers and the baseline blade chord, a total of 11 parameters define the overall blade geometry. This parameterization can be simplified or modified as needed; the example presented in this paper is intended to show just a representative case of the approach.

### B. Airfoil Database Definition

The couplings between planform and airfoil shape result in a nonuniform spanwise camber and thickness ratio distribution whenever a nonrectangular blade shape is considered. Hence, it is necessary to obtain the sectional aerodynamic characteristics of the various airfoils along the span to implement a strip-based aero dynamic model of the blades. Similarly, the local chord and radial position along the blade determine the local $Re$ that each blade section encounters. Because one of the main motivations of the current research is to develop an approach that can be applied to the design and analysis of a wide range of vehicles, lift and drag coefficients for each geometry need to be specified over a range of $Re$ and angles of attack.

The range of cambers included in the database was discretized in steps of 1.5%, resulting in seven airfoil geometries with a thickness ratio of 2.5%. Each airfoil shape can potentially face the largest or the smallest $Re$ that the NAV or MAV encounters; hence, the sectional characteristics for each airfoil have to be obtained over the specified $Re$ range of 5000–60,000. Airfoil characteristics were calculated at the specific $Re$ values of 5000; 10,000; 15,000; 20,000; 30,000; 45,000; and 60,000. Table 1 shows the extents of the database. Each of the lift and drag curves in the database extends from −4 to 14 deg angle of attack. As explained in more detail in the model implementation section, this is an appropriate range to achieve conver gence in most scenarios.

The database discretization along its various dimensions allows the aerodynamic coefficient at any angle of attack, $Re$, and geometry to be obtained within or in the vicinity of the database boundaries by using an interpolation/extrapolation scheme. In this way, a model

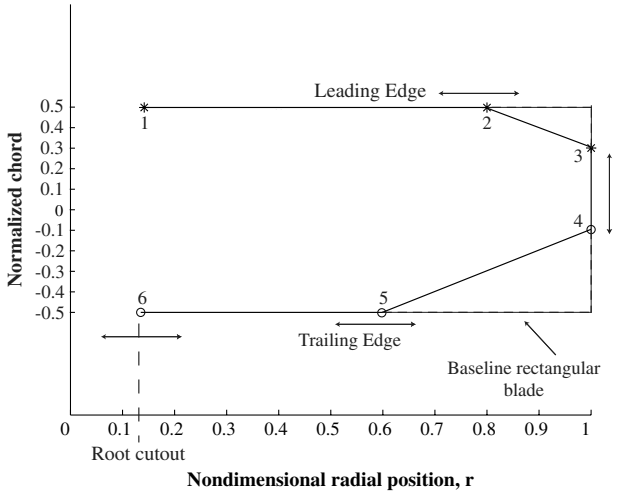


**Fig. 4 Blade planform definition.**

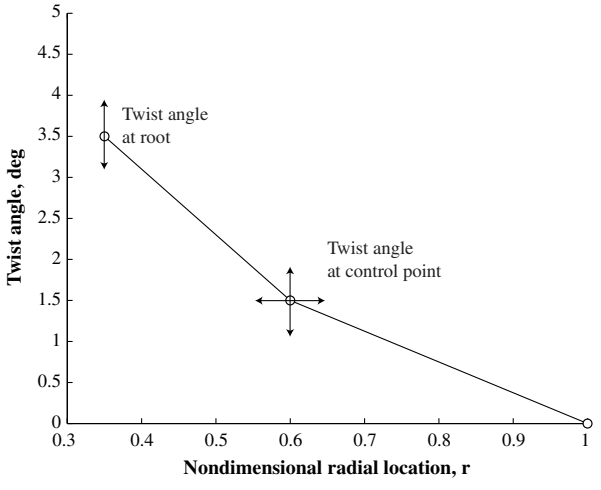


**Fig. 5 Two-section linear twist distribution.**

**Table 1 Test matrix for CFD calculations, combinations of camber and *Re***

| | Camber | | | | | | |
|---|---|---|---|---|---|---|---|
| *Re* | 0% | 1.5% | 3.0% | 4.5% | 6.0% | 7.5% | 9% |
| 5000 | √ | √ | √ | √ | √ | √ | √ |
| 10,000 | √ | √ | √ | √ | √ | √ | √ |
| 15,000 | √ | √ | √ | √ | √ | √ | √ |
| 20,000 | √ | √ | √ | √ | √ | √ | √ |
| 30,000 | √ | √ | √ | √ | √ | √ | √ |
| 45,000 | √ | √ | √ | √ | √ | √ | √ |
| 60,000 | √ | √ | √ | √ | √ | √ | √ |

that uses the database and the proposed blade parameterization can be applied over a wide range of blade geometries, configurations, and operating conditions without additional aerodynamic data.

## IV. Experimental Rotor Characterization: Ground Truth Data

The ground truth data used to validate the model predictions were generated using rotor diameters of 210 and 75 mm, which are representative of MAV- and NAV-scale vehicles, respectively. In both cases, experiments with rectangular and tapered blades were performed using untwisted rectangular baseline blades with a uniform spanwise camber. For each rotor configuration, a series of angles of attacks and rotational speeds were explored. Table 2 summarizes the test matrix for the rectangular blades, and Table 3 the tests for the tapered blades.

The tests cover a *Re* range that extents from about 10,000 to 40,000 at 75% of the span. However, when considering the inner and outer blade regions, the Reynolds numbers range of interest extends from 5000 up to 50,000. This is in agreement with the extents of the proposed airfoil database to be used in the model implementation.

The MAV- and NAV-scale rotors were manufactured using different processes and materials. The smaller and lighter NAV-scale rotors were manufactured using a rapid prototyping machine, an Objet Eden350$^{TM}$ that used FullCure® 840 VeroBlue as printing material. For these rotors, hub and blades are manufactured as a single piece, each collective requiring a different rotor. The main advantage of this method is the ease of manufacturing and high accuracy of airfoil shapes and blade pitch settings. The larger MAV-scale rotors were manufactured following a more traditional procedure: blades were made of a multilayered carbon fiber prepreg and cured on aluminum molds. An aluminum hub held the composite blades and pitch was set manually with an uncertainty of less than a quarter of a degree.

### A. Experimental Setup

An experimental setup designed to measure the hover performance of small-scale rotors was developed. The stand simultaneously measures thrust, torque, and rotational speed; these are the quantities required to calculate figure of merit and power loading of the hovering rotors. Torque is measured using a RTS-5 5 oz · in. torque cell by Transducer Techniques, and thrust is measured using a Model 31, 1000 g precision tension/compression load cell by Sensotec. The torque cell is mounted on a baseplate, and the load cell is mounted in a fixture on top of the torque cell. The components of the load cell fixture are either anodized aluminum or plastic, with the exception of the spindle support diaphragms, which are tempered spring steel. The load cell fixture transfers the rotor torque directly to the torque cell and ensures that only vertical (rotor thrust) loads are transmitted to the load cell. The rotor system, including rotor, motor, and gearbox, is mounted on a stinger on top of the load cell fixture. Figure 6a shows the exploded diagram of the test stand, and Fig. 6b shows a picture of the hover test stand. Rotor rpm is measured using a Hall effect sensor that detects the passing of small magnets mounted on a rotating component of the rotor system. The motors are powered using a Sorensen DLM20-30 power supply.

**Table 3 Test matrix for tapered rotors**

| Baseline camber | Rotor diam | Taper ratio | Taper start |
|---|---|---|---|
| 4.5% | 75 mm | 2:1 | 0.8*R* |
| 6% | 225 mm | 2:1, 1.66:1, 1.33:1 | 0.8*R* |
| 9% | 225 mm | 2:1, 1.66:1, 1.33:1 | 0.8*R* |

The data from the test stand were collected using an electronic data acquisition system. A National Instruments DAQcard-6062E and a SC-2345 carrier box with NI-SCC modules were used for signal conditioning and data collection. A custom code specifically tailored for these experiments was developed in MATLAB and run on a laptop PC. The code was designed to simultaneously acquire up to eight channels while sending up to two analog control signals. The sampling rate for all tests was 5000 samples per second for each channel. A proportional–integral controller was embedded in the software to control the motor's rotational speed using the output from the Hall effect sensor as feedback.

### B. Experimental Results: Rectangular Blades

Experimental measurements are used to calculate the hover performance of the rotors tested in terms of figure of merit (FM) and power loading (PL). These results are useful not only to illustrate the basic trends in rotor performance but were used to gain a clear understanding of the criteria to be used when optimizing the design of a hovering rotor.

#### 1. *Micro-Air-Vehicle-Scale Results*

Figure 7 shows the $C_T$ vs $C_P$ plots for the various MAV rotors at 2500 rpm; this corresponds to a *Re* of 32,700 at 75% of the span. Camber clearly influences the thrust produced and the power required by the rotors over the range of collectives explored. Using these coefficients to calculate FM, the curves in Fig. 8 were generated. This plot shows the positive influence of camber on maximum FM. As expected, the poorest performance in terms of FM was obtained with the flat plates that reach a maximum FM of only

**Table 2 Test matrix for rectangular bladed rotors**

| Rotor geometry | Camber, % | $\alpha$, deg | Rotor speed, rpm | *Re*, 75% span |
|---|---|---|---|---|
| | | *MAV-scale rotors* | | |
| Diam: 225 mm<br>Chord: 22.5 mm<br>$\sigma$: 0.1279<br>Root cutout: 13.5% R<br>Airfoil TR: 2.2% | 0, 3<br>6, 9 | 0–18<br>In steps of<br>2 deg | 2000, 2500, 3000 | 26,200; 32,700; 39,300 |
| | | *NAV-scale rotors* | | |
| Diam: 75 mm<br>Chord: 10 mm<br>$\sigma$: 0.1279<br>Root cutout: 13.5% R<br>Airfoil TR: 2.2% | 0, 3, 4.5<br>6, 7.5, 9 | 0–18<br>In steps of<br>2 deg | 5000; 7500; 10,000 | 9700; 14,600; 19,500 |

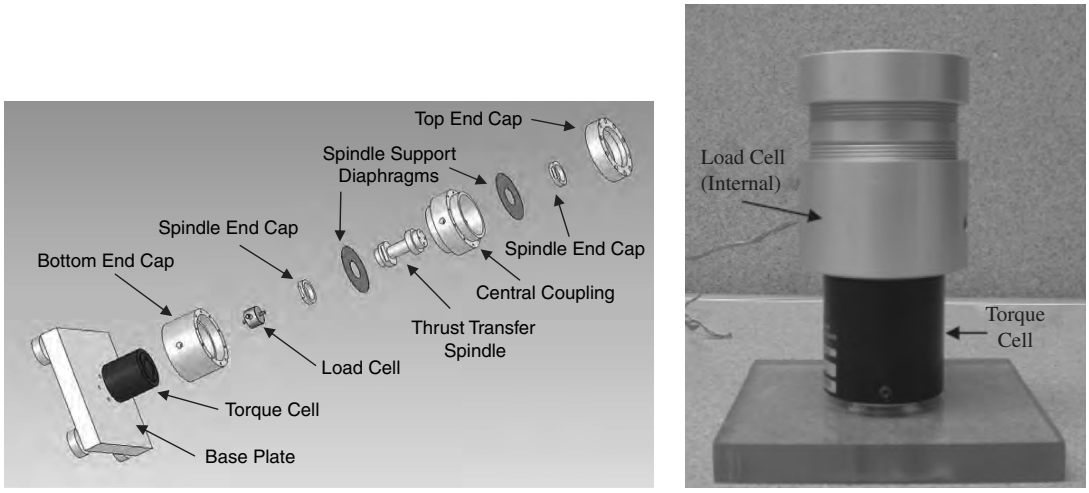


**a) Diagram of exploded hover stand** **b) Hover stand**

**Fig. 6 Hover stand used for experimental measurements.**

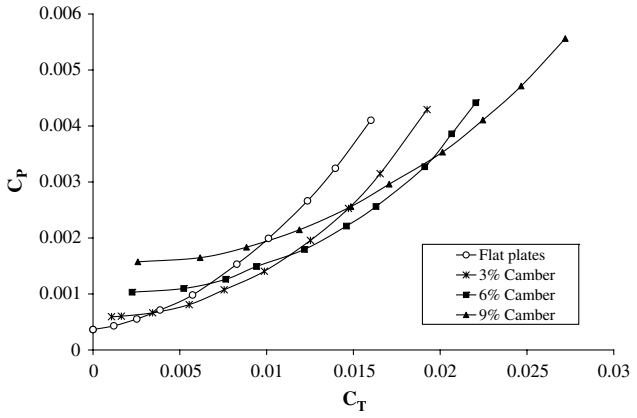


**Fig. 7 $C_T$ vs $C_P$ at 2500 rpm for rotors with circular arc airfoils of various cambers and elliptical LE, $c = 2.25$ cm and TR = 2.2%, tip $Re = 43,700$.**

0.36. With the 3% camber blades, the maximum FM increased to 0.51, which is a 41% increase. A moderate but still significant improvement occurred with the 6% camber blades that reached a maximum FM of 0.57, just 1 percentage point below the global maximum FM of 0.58 measured with the 9% camber blades. Another important trend to notice is the gradual shift to higher collectives and $C_T$ values of maximum FM as camber is increased.

Figure 9 shows the experimental MAV-scale results using PL as efficiency metric and having rotor disk loading (DL) as abscissa. By doing the same quantitative comparisons as the $C_T$ vs FM plots, it would seem at first sight that there is a contradiction in the observed trends when looking at the maximum PL values: maximum PL is highest with the 3% camber blades rather than with the 9% camber ones. However, the local maximum for each rotor occurs at very different values of DL. In fact, FM and PL comparisons are valid only when DL is kept constant. Hence, these results only show how, at a particular DL, the 3% camber blades produce a higher thrust per unit power than the other rotors, although they have a relatively low maximum FM. A detailed interpretation of these results is given in a following section, in which the criteria for rotor efficiency comparison is discussed.

*2. Nano-Air-Vehicle-Scale Results*

The measurements on the NAV-scale rotors follow similar trends as the MAV measurements; however, the effects of camber on maximum FM and maximum $C_T$ are less pronounced. Figures 10 and 11 show the experimental results for all of the rotors at 10,000 rpm; this corresponds to a $Re$ of 19,500 at 75% of the span. Most of the rotors have a maximum FM of approximately 0.45 at a $C_T$ of around 0.017, the only exceptions being the flat plates, which have a maximum FM of 0.34, and the 9% camber blades, which have a maximum FM of 0.47 at a $C_T$ of 0.0216. Comparisons of the results in terms of PL are shown in Fig. 12. Overall hover efficiency of the NAV rotors was considerably lower than that of the MAV rotors in terms of the maximum FM and PL. This is an expected result considering the lower rotor area, higher rotational speeds, and lower operating $Re$ of the NAV rotors.

### C. Experimental Results: Nonrectangular Blades

A few representative MAV and NAV rotors with simple linear asymmetric tapered blades were tested. These geometries were

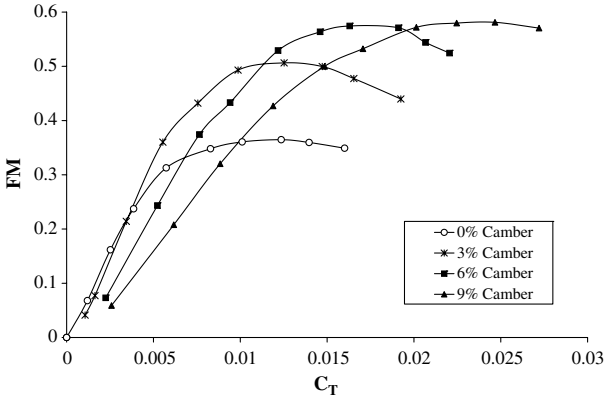


**Fig. 8 $C_T$ vs FM at 2500 rpm for rotors with circular arc airfoils of various cambers, tip $Re = 43,700$.**

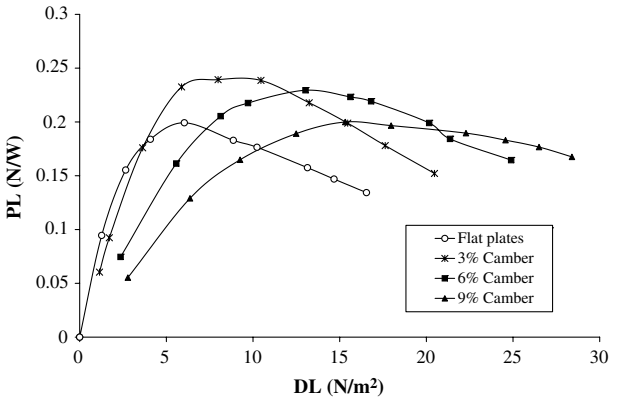


**Fig. 9 $C_T$ vs $C_P$ at 2500 rpm for rotors with circular arc airfoils of various cambers, tip $Re = 43,700$.**

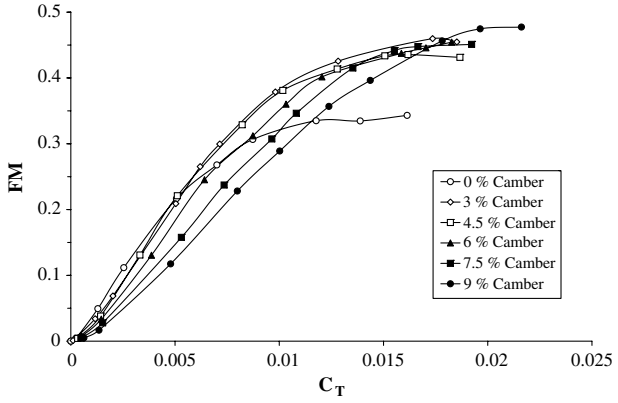


**Fig. 10 $C_T$ vs FM at 10,000 rpm for NAV-scale rotors.**

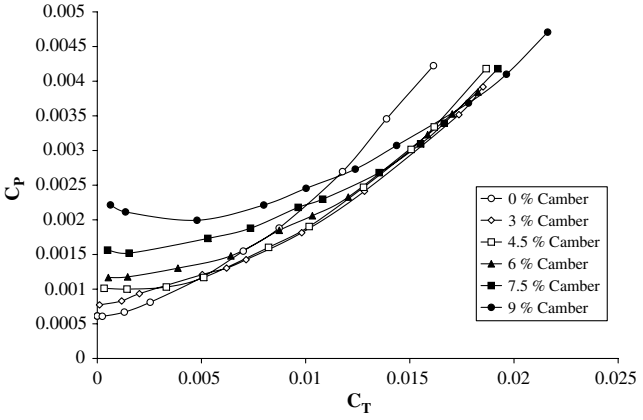


**Fig. 11 $C_T$ vs $C_P$ at 10,000 rpm for NAV-scale rotors.**

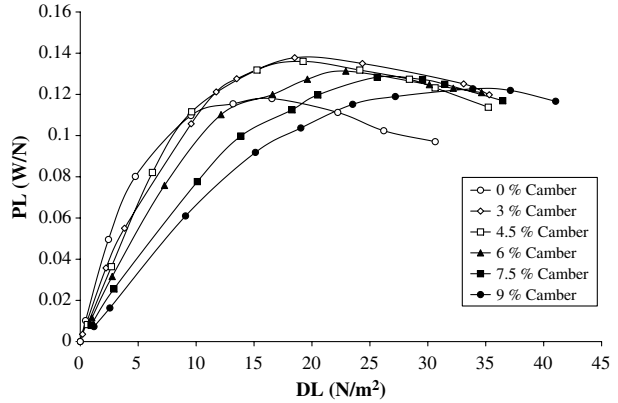


**Fig. 12 DL vs PL at 10,000 rpm for NAV-scale rotors.**

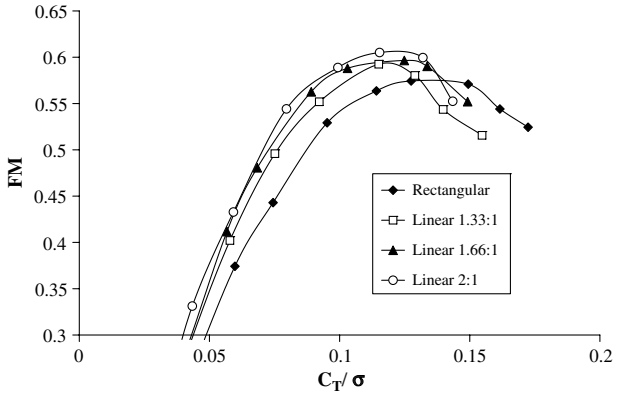


**Fig. 13 $C_T/\sigma$ vs FM for baseline 6% camber rotors and various taper ratios at 2500 rpm.**

obtained by removing blade material from the trailing edge only, cutting between points 4 and 5 of Fig. 4. For the MAV blades, baseline cambers of 6 and 9% were tapered using three ratios (2:1, 1.66:1, and 1.33:1). For the NAV rotors, a 4.5% baseline camber with a 2:1 taper ratio was chosen. In all cases, taper started at $0.8R$.

As for the sample case of Fig. 3, the removal of material from the trailing edge introduced a linear camber reduction and negative twist along the tapered regions of the blades. A reduced blade tip area with lower cambers and angles of attack results in a lower lift and reduced inflow at the outer blade regions, shifting the $C_T$ vs FM curves to the left. Figures 13–15 show the experimental FM curves plotted vs blade loading ($C_T/\sigma$).

The effect on maximum hover efficiency was favorable in all cases. For the 6% camber rotors, the 2:1 taper ratio resulted in a maximum FM of 0.6 at 14 deg collective. This is an improvement of 5% over the baseline. For the 9% baseline camber blades, the highest FM was achieved again with a 2:1 taper ratio, reaching a maximum FM of 0.62, which is an almost 9% increase over the rectangular blades. Measurements with the NAV-scale rotors show a similar trend (Fig. 15). Maximum FM had a moderate increase from 0.43 at 16 deg collective to 0.45 at 18 deg collective, which is a change of 4%.

These representative experiments show that the geometric blade modifications proposed have a clear and measurable effect on the performance of both MAV- and NAV-scale rotors. The trends identified in this section are used to validate the model implementation used for the optimization of rotor blades.

### D. Hover Performance Metrics

At small scales, vehicle characteristics and operating conditions can vary widely, making rotor design a very involved task. Hence, to systematically compare rotors, it is key to understand the limitations of the hover efficiency metrics.

Up to this point, results have been compared keeping rotational speed and rotor diameter constant between the measurements. When

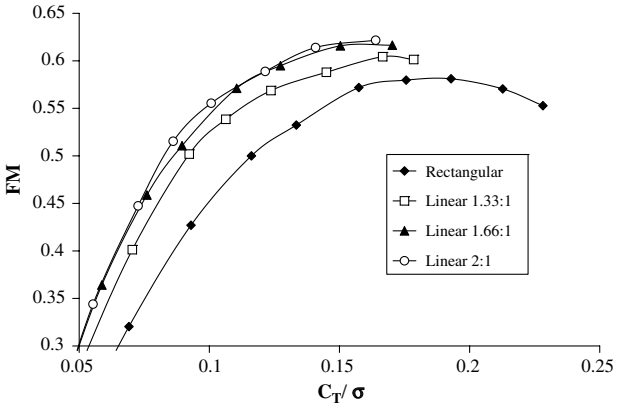


**Fig. 14 $C_T/\sigma$ vs FM for baseline 9% camber rotors and various taper ratios at 2500 rpm.**

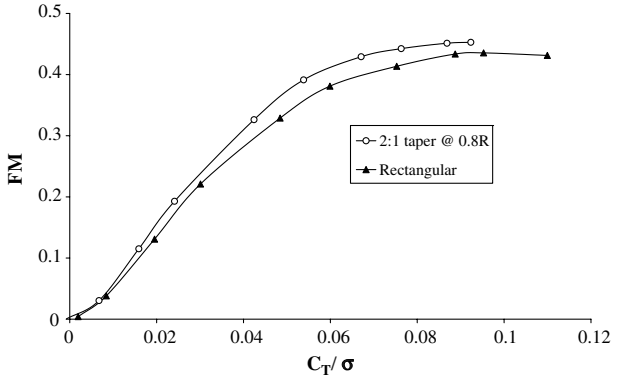


**Fig. 15 $C_T/\sigma$ vs FM for baseline 4.5% camber NAV-scale rotors and 2:1 taper ratio at 10,000 rpm.**

this is the case, as in Figs. 8 and 9, the best airfoil choice depends on the DL or $C_T$ at which the rotor needs to operate. This is the simplest design scenario, where the rotor with highest FM or PL at the operating $C_T$ or DL is the best choice. However, when either the rotational speed or rotor diameter is a design parameter, which is typically the case whenever a new vehicle is developed, finding the best choice within a pool of configurations is not as straightforward. For this case, the use of FM can be misleading given that two rotors spinning at different speeds can have the same $C_T$ but different DL, and performance comparisons in terms of FM and PL have to be done at equal DL to be valid.

To systematically compare rotors at various operating conditions, hover performance data over a range of collectives and rotational speeds need to be available. When plotting FM vs $C_T$ for a range of rotational speeds, as in Figs. 16 and 17a, it can be observed that the maximum FM values gradually decrease as rotational speed is lowered. However, because even at the same $C_T$ the DL is different for each curve, no direct comparisons can be performed. An unambiguous approach is to use PL (cf. [5]), as in Figs. 16b and 17b. These two figures show the same experimental data using PL vs DL. This format clearly shows the difference in operating conditions of the various tests while providing valid hover efficiency comparisons. For each rotational speed, the maximum PL is achieved at a collective below the one that maximizes FM; however, when considering the entire set of curves over a range of disk loadings, the envelope for maximum PL (shown by a dotted line in Fig. 16a) is defined by the curve that connects the power loadings at maximum figures of merit over the range of rotational speeds considered. Therefore, to choose the rotor that minimizes the power requirements for a given thrust, the envelopes of maximum power loading of the configurations considered should be compared. This is the criteria that is used in the optimization code implemented for this research.

A good example of how the envelope for maximum PL is used to compare various rotor configurations is shown in Fig. 18, where the

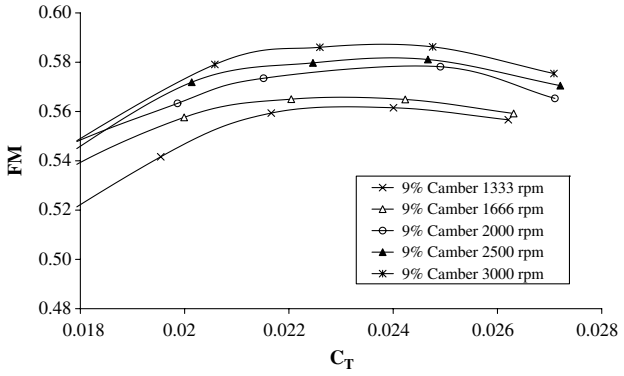


**a) $C_T$ vs. FM for various RPM, 12 to 18deg collective**

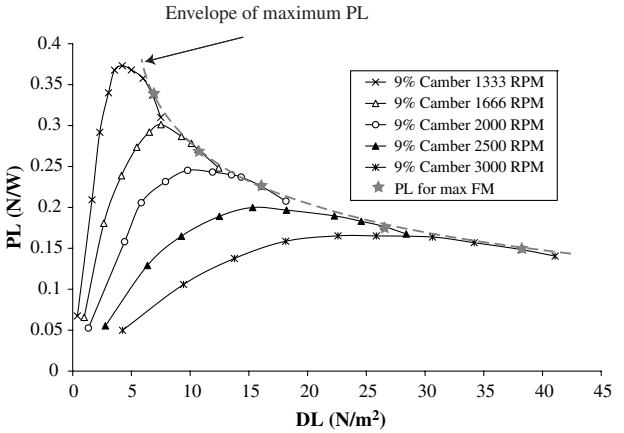


**b) DL vs. PL various RPM - envelope of max PL**

**Fig. 16 Hover performance of rotor with 9% camber rectangular blades at various rpm.**

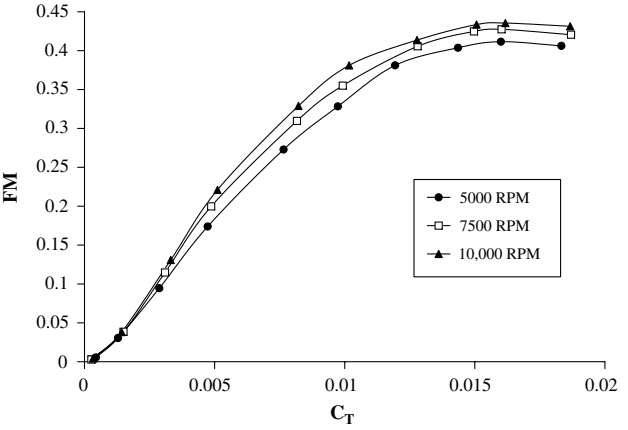


**a) $C_T$ vs. FM**

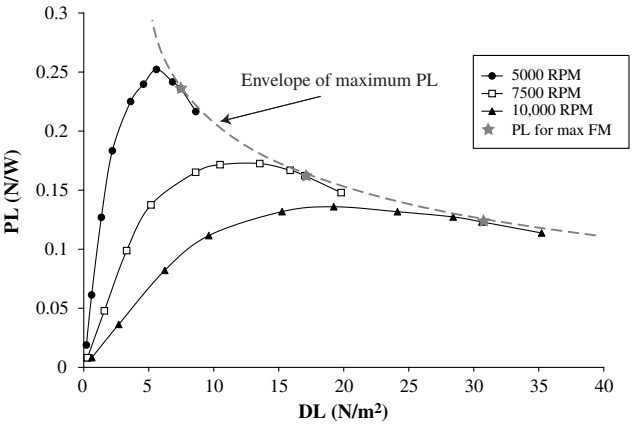


**b) DL vs. PL**

**Fig. 17 Experimental performance measurements of NAV-scale rotor with 4.5% camber airfoils at various speeds.**

curves of MAV-scale rotors with rectangular and tapered blades (2:1 ratio) are plotted simultaneously. Performance comparisons over a range of DL are straightforward without creating any confusion related to variations in rotational speed.

## V. Hovering Rotor Model Implementation

Blade element momentum theory is a powerful tool used to model the aerodynamics of hovering rotors. The fundamental equations and derivations for BEMT are found in [13], as well as in [4,14]. BEMT is based on a discretization of the rotor disk in a series of concentric rings that are assumed to have no mutual effect on each other. Blade sections included in each ring can have different aerodynamic coefficients, chord, and pitch, allowing complex blade geometries to

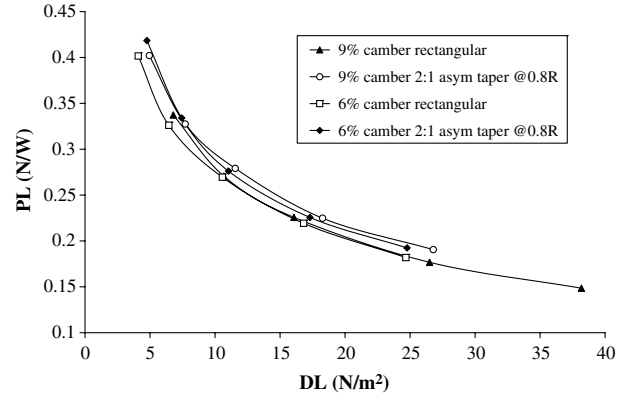


**Fig. 18 Maximum PL envelope for various MAV-scale rotors.**

be modeled. BEMT is very inexpensive computationally and is ideal for the implementation of a table lookup scheme that uses the circular arc database defined previously. The most straightforward application of BEMT is the analysis and design of rotors; however, it can also be used to validate, rectify, and even generate the aerodynamic sectional lift and drag characteristics of airfoils. Historically, for full-scale application, reliable airfoil data are easily found, and simplifying assumptions like constant lift coefficient slopes or a constant drag coefficient are commonly used. At low Reynolds numbers, airfoil data are scarce and unreliable, and thus, as opposed to full scale, it is much simpler to perform rotor hover testing than wind-tunnel measurements. In the current investigation, a BEMT rotor model is used both ways: first to validate and calibrate the airfoil database, and second to analyze and optimize hovering rotors at various operating conditions.

### A. Airfoil Sectional Characteristics from Hover Rotor Tests

To obtain airfoil characteristics from rotor tests, untwisted rotors having rectangular blades and a uniform airfoil along the span should be used. For that particular case, analysis can be simplified by considering a single set of lift and drag coefficient curves ($C_l$ and $C_d$ vs $\alpha$) at the Reynolds number found at 75% of the blade span. In the BEMT numerical implementation, the local lift and drag coefficients along the various blade sections are interpolated based on the in duced angles of attack that are iteratively obtained from the inflow calculations. By gradually increasing the collective pitch of the blades from a small angle (close to the rotor zero-lift condition) up to collectives beyond the operating point of the blades, the entire range of interest of the lift and drag coefficients is gradually covered. The BEMT implementation uses Prandtl's tip loss function [13] to model the lift reduction resulting from the higher tip local inflow. This approach increases the inflow to obtain a zero-lift condition at the blade tip. Hence, for all collectives, the range of induced angles of attack along the span typically has a lower bound than the zero-lift angle of attack of the airfoil used.

To validate, rectify, and even generate the lift and drag sectional coefficients of a given airfoil, the BEMT model predictions of rotor thrust and power coefficients ($C_T$ and $C_P$) can be compared to experimental rotor hover performance measurements using the same closely spaced collective increments. Lift and drag curves can be modified in segments until there is complete agreement between numerical and experimental results at all collectives and rotational speeds. Figure 19 shows the algorithm followed to generate the aerodynamic coefficient curves. Rotor geometric parameters and operating conditions are needed as inputs, as well as an initial guess of the $C_l$ and $C_d$ vs $\alpha$ curves. Using the initial guess of the airfoil's $C_l$ vs $\alpha$ function, the rotor thrust coefficient $C_T$ is calculated for each collective pitch setting starting from a collective that will produce a minimum of thrust. For each rotor collective, the blade span faces a range of angles of attack (as shown later). For the lower collectives, where little thrust is produced, the range of lift and drag coefficients covered is relatively small, spanning just a few degrees. As the blade collective is increased, the $C_l$ and $C_d$ range gradually expands. Hence, accuracy of the corrections improves with the density of the experimental blade pitch discretization. Model predictions are compared with the experimental ones and are then modified, depending on the sign of the error the $C_l$ vs $\alpha$ curve. Changes in slope and/or magnitude are introduce to the baseline coefficient curves making sure that the final result is continuous and consistent with airfoil behavior.

Drag coefficient calculations must follow the determination of the lift coefficients because there is an induced component in the total power required by the rotor that will directly depend on the lift characteristics of the airfoil. As for the thrust coefficients, the numerical and experimental power coefficients are compared, adjusting the $C_d$ vs $\alpha$ curve until good agreement is reached.

### B. Rotor Optimization Algorithm

The simplest implementation of a BEMT rotor model would use linear aerodynamics (independent of the spanwise variation in operating conditions) to find the sectional lift and drag coefficients needed for performance calculation. A higher level of sophistication involves interpolating actual aerodynamic curves that can have up to three dimensions: angle of attack, $Re$, and $M$. For the database used in this investigation, each airfoil has two dimensions to interpolate: angle of attack and $Re$. Taking into account that the database covers a range of cambers, a total of three parameters need to be specified to find the lift and drag coefficients at each blade section.

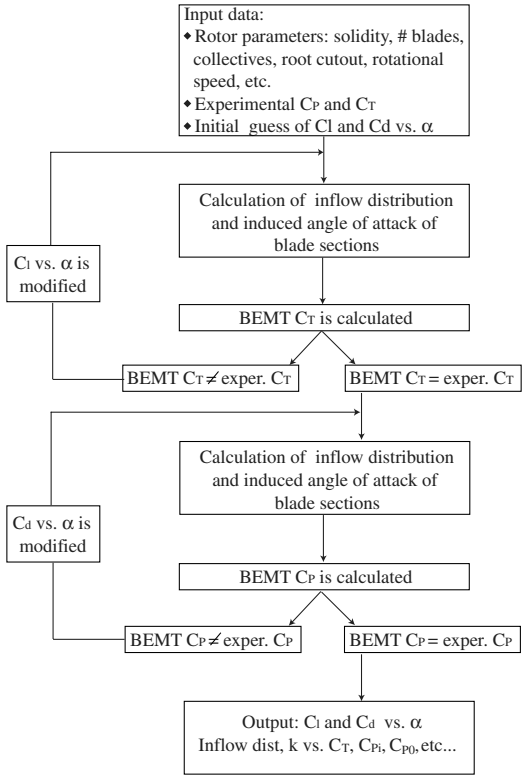


**Fig. 19 Algorithm used to obtain average airfoil characteristics from rotor tests using BEMT.**

The BEMT model was coupled with the database defined in Sec. III.B, allowing the performance of rotors within the design space to be calculated. The model needs input of basic rotor geometric parameters such as diameter, number of blades, and root cutout, as well as operational parameters like rotational speed and collective. In addition, the blade geometry needs to be specified following the parameterization proposed in Sec. III.A. This application of the model is useful for rotor analysis, because it returns the rotor thrust and power requirements for the specified inputs.

If the model is intended to be used as a design tool, an optimizer can be introduced to the algorithm as shown in the block diagram in Fig. 20. In this case, the design requirements and specific bounds of the design space need to be given to the code. The basic design requirement is generally the rotor thrust determined by the gross takeoff weight or maximum climb speed of the vehicle. Additional constraints will bound the design space over which the search for the best configuration is carried out. These constraints specify the parameters that define the geometry or the operating conditions of the rotors, and they can either have a fixed value or vary within a certain discretized interval.

The optimization is divided in two steps. A first step consists of a grid search of the design space defined by the constraints, finding the power consumed and collective required by each configuration at the required thrust. The number of runs depends on the number of variables and the number of values that each variable takes over the defined intervals. After the grid search is complete, the best performing rotor is found using PL as a performance metric. The operational and geometric parameters of the best performing rotor are then used as an initial guess value in a constrained nonlinear optimization coded in MATLAB. The results of the second

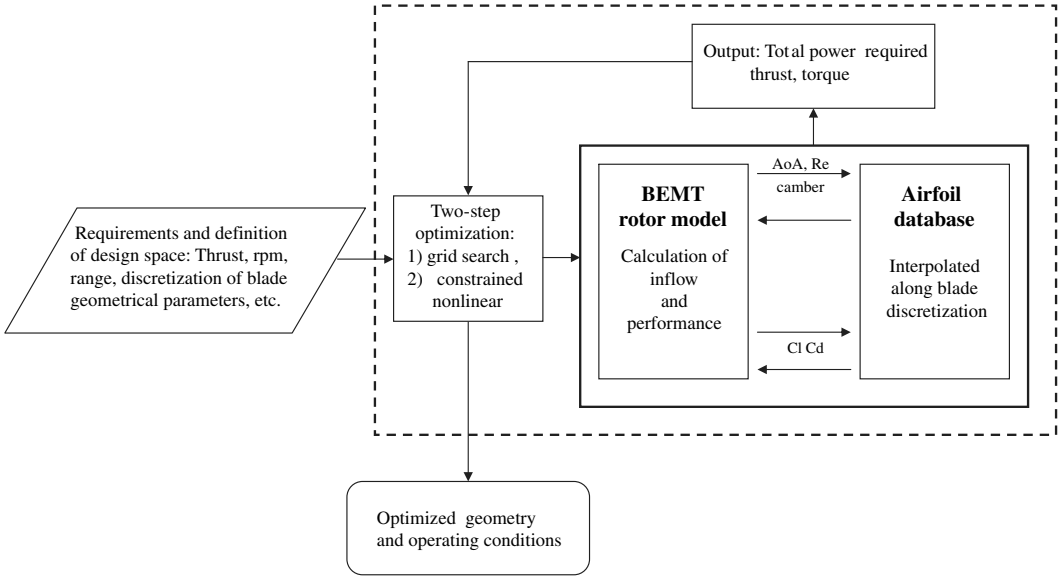


**Fig. 20 Block diagram of optimization algorithm.**

optimization stage is a refined set of parameters that maximizes the PL at the specified thrust within the bounds of the design space. Depending on the grid density, the second step might provide only marginal improvements.

## VI. Two-Dimensional Airfoil Database Calculation

To accurately predict the performance and optimize the design of small-scale rotors, it is necessary to obtain the sectional lift and drag coefficients of the airfoils used. For the research presented in this paper, aerodynamic coefficients are obtained using a two-step hybrid method that first uses two-dimensional CFD to calculate the baseline airfoil coefficients and then applies empirical corrections based on the measured hover performance data (as explained in Sec. V.A) to refine the database.

### A. CFD Methodology

This section explains the grid generation methodology, the flowfield assumptions, and the boundary conditions used for the calculations of two-dimensional airfoil characteristics.

#### *1. Flow Solver*

The flow solver used for the CFD calculations was INS2d, an incompressible Navier–Stokes solver developed by Rogers and Kwak [15,16]. The code solves the incompressible Navier–Stokes equations in two dimensions using the method of artificial compressibility and an implicit line-relaxation scheme. The flow solver INS2D has been previously used at low-$Re$ regimes by Kunz and Kroo [17,18], who performed an airfoil camberline optimization at extremely low Reynolds numbers assuming fully laminar flow. Their work focuses on a $Re$ range that covers only a small fraction of the design space relevant for this investigation. Because fundamental flowfield assumptions were different, their results were not used for validation.

#### *2. Grid Generation*

Grid generation is an essential aspect of all numerical methods that use finite differences, finite volumes, or finite elements to solve partial differential equations. For the current research, a hyperbolic grid algorithm that generates structured $C$-type grids was used.

The computational cost of two-dimensional grid generation is minimal when compared to the total computational cost of the flow solution. In the algorithm used, a clustering factor was specified to increase the grid density at the leading and trailing edges. A representative grid would have about 25 cells along the upper and lower surfaces (50 cells total) from the leading edge up to 5% of the airfoil chord. Initial normal spacing was set to obtain approximately 25 cells in the boundary layer. The airfoil geometry was generated using the same parameters used by Mueller in [12] and shown in Fig. 2. This airfoil family has an elliptical leading edge for which the length is defined as a function of the airfoil thickness.

Figure 21 shows the grid around a curved plate airfoil showing the clustering at the leading and trailing edges. All the grids used in this investigation had a $J_{\max}$ of 217 points and a $K_{\max}$ of 81 points. The airfoil contour was defined with 160 points leaving 57 points for the definition of the wake-cut boundary. The outer grid radius was placed at 15 chord lengths. A simple grid sizing study was performed by increasing the $J$ and $K$ grid dimensions in three steps: $109 \times 41$, $217 \times 81$, and $435 \times 163$. The relative errors in lift and drag coefficients were calculated with respect to the results of an $871 \times 327$ grid using a 4% camber circular arc at 60,000 $Re$. The $217 \times 81$ grid had a relative error close to 0.5% in lift and drag. This grid was chosen because it offers a good compromise between error and computational cost.

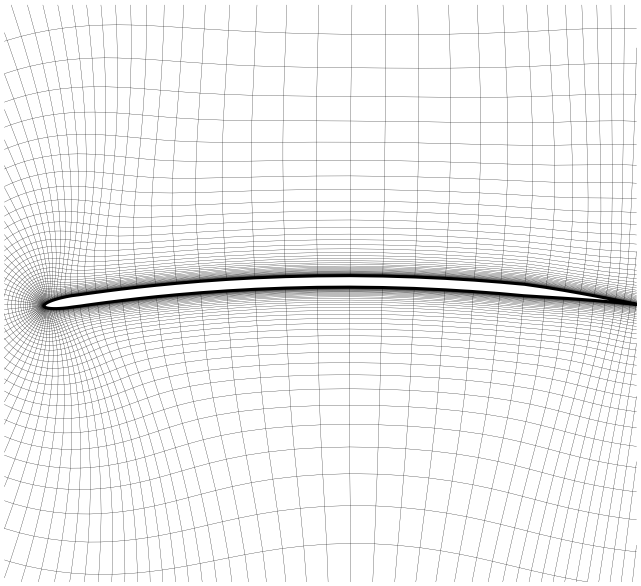

**Fig. 21 Sample grid around a curved plate airfoil showing clustering at leading and trailing edges.**

*3. Boundary Conditions*

The solver uses a viscous no-slip wall at the surface of the airfoil, with the wall-normal vector pointing in the positive computational direction. At the outer *C*-grid boundary, INS2D divides the outer boundary in two: a section that imposes a velocity field based on freestream velocity, and another that specifies the outflow using extrapolated velocity and constant static pressure. It is also necessary to specify a wake-cut boundary condition where the points are updated by averaging the values of its surroundings.

*4. Flowfield Assumptions*

Three main flowfield assumptions were used. The flow was assumed to be fully turbulent, steady, and incompressible.

In the *Re* range under consideration, it is expected that the flow is either laminar and undergoes separation, or transitional with laminar and turbulent sections. With the current CFD state of the art, it is not possible to model transition; however, three different approaches are possible: the flow can be assumed to be either fully laminar or fully turbulent, or a specified chordwise transition location can be used. Of these three options, the assumption of a fully turbulent flow seems the most convenient choice. Fully turbulent calculations minimize the computational cost and allow one to have some general CFD results without going into detailed modeling of the boundary-layer behavior. Considering the large number of airfoils, angles of attack, and *Re* to evaluate, it was impractical to follow a different approach with the computational resources available. When turbulent flow is assumed, it is necessary to calculate the turbulent viscosity using a turbulence model. Based on previous investigations [19–21], it was decided to use the one-equation model of Spalart and Allmaras [22]. In its original form, the Spalart–Allmaras model is effectively a low-Reynolds-number model, requiring the viscous-affected region of the boundary layer to be properly resolved. An additional advantage is that its relative simplicity minimizes computational costs, making it particularly well suited for a large number of calculations when limited computing power is available.

The steady assumption may be an oversimplification of the problem, particularly at the higher angles of attack where separation occurs. Some wind-tunnel experimental investigations (cf. [23]) have identified periodic vortex shedding in airfoils under similar conditions. This may be one of the reasons why it is necessary to introduce substantial empirical corrections to the numerical CFD results to achieve good correlation with rotor experiments. Unsteady CFD runs were prohibitive due their high computational cost, and, because the objective of this investigation is to develop a methodology that minimizes computational resources while maximizing predictive accuracy, only steady flow calculations were performed.

Finally, the third flow characteristic to model is its compressibility. Considering that the highest tip Mach number reached by the rotors is below 0.3, it is reasonable to assume incompressible flow.

### B. Computational Fluid Dynamics Validation

The CFD results were validated using data from wind-tunnel experiments performed at a *Re* of 60,000 on a circular arc airfoil with 4% camber and 1.93% TR, matching the proportions shown in Fig. 2. The wind-tunnel experiments were performed by Mueller [12] at the Hessert Center for Aerospace Research, University of Notre Dame, and the resulting report is one of the few reliable aerodynamic studies of thin circular plates in the literature. The Reynolds number of the experiments is an upper bound of the aerodynamic regime faced by

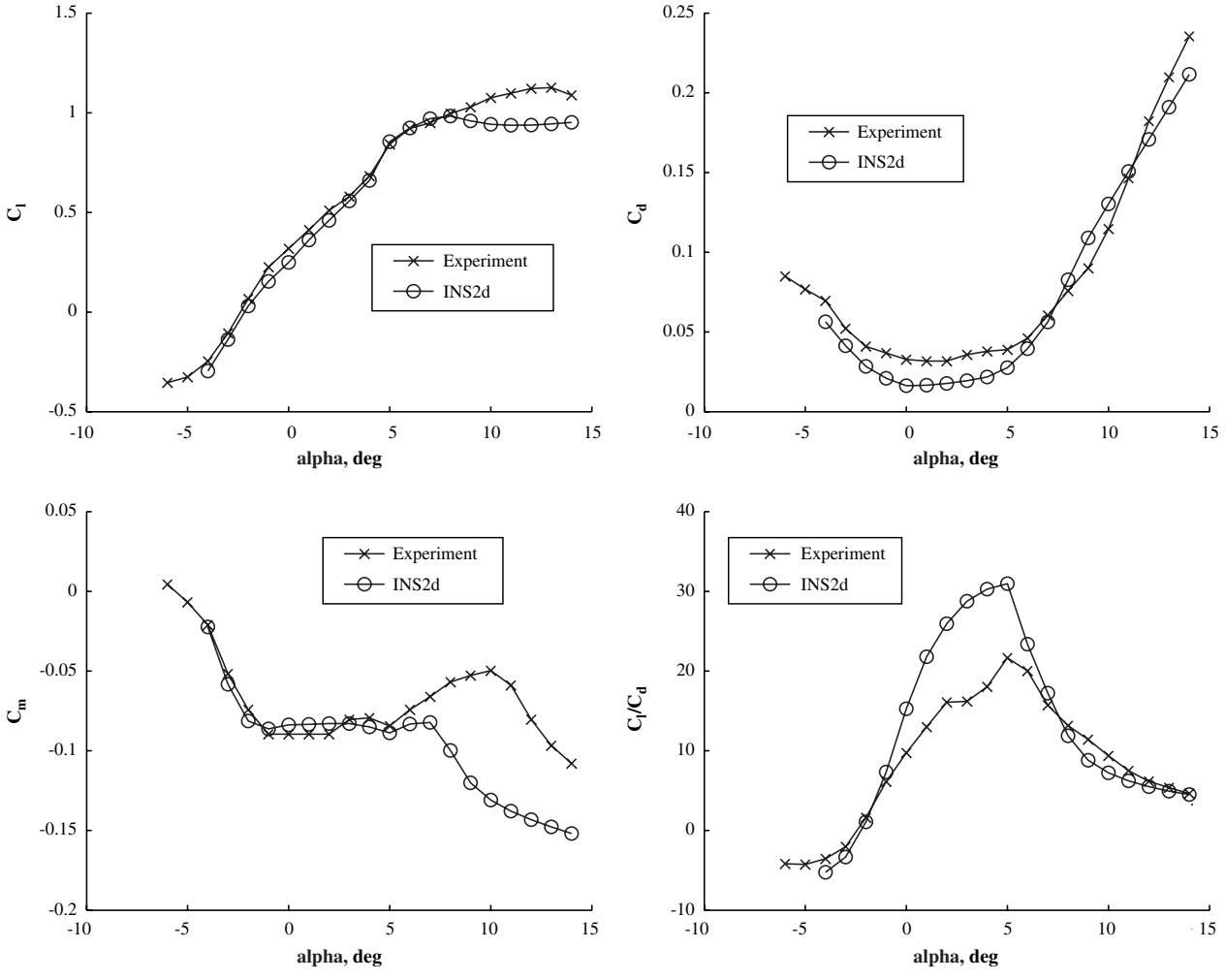


**Fig. 22 Lift, drag, moment, and lift-to-drag ratio validation INS2d, with experimental data at $Re = 60,000$ from [12].**

MAVs. Nevertheless, due to the limited availability of experimental data, Mueller's results were used for validation.

Figure 22 shows the experimental and predicted lift, drag, and moment coefficients as well as the lift-to-drag ratio obtained with INS2D. The lift coefficient curves have a good agreement over most of the angles of attack explored. However, the code predicts an early stall.

The solver underpredicted drag at the lower angles of attack by as much as 50% over the region from $-1$ to 4 deg. These differences translate into large errors in the lift-to-drag ratio predictions. Whereas the experimental maximum $L/D$ is 23, computational results predict an $L/D$ of 31. Nevertheless, INS2d accurately predicts the angle of attack for maximum lift-to-drag ratio.

The large differences in the computational drag predictions, as noted by Schroeder and Baeder [19] and Lakshminarayan et al. [21], seem to be a consequence of the fully turbulent flow assumption. At low angles of attack, the turbulence model is likely to underpredict the length of the separation bubble and possibly the extent of regions of separated flow at the lower surface of the airfoil, where, at low angles of attack, large adverse pressure gradients exist.

As discussed by Mueller [12] and Barber [24], the lift and drag wind-tunnel measurements can be affected by the presence of end plates. These are used when two-dimensional flow is desired. The interaction between the end plate's boundary layer and the flow around the wing creates a corner flow that can largely increase the two-dimensional drag measured. At Reynolds numbers between 60,000 and 200,000, Mueller and Jansen [25] show an increase in the measured minimum drag coefficient of 18% when end plates were used. These unresolved experimental issues make the validation of codes and models difficult (cf. [26]).

## VII. Model Results

Performance predictions with two model implementations were performed. For the MAV-scale rotors, the CFD-calculated database was used for the coefficients interpolation, whereas for the NAV-scale rotors, the empirically corrected database was used. More specifically, for the NAV-scale rotors, the relevant regions of the CFD-calculated database, defined in Table 1, were empirically corrected to improve the model's predictive capabilities.

### A. Micro-Air-Vehicle-Scale Results: Unmodified Database

The CFD-calculated database coupled with a BEMT rotor model was used to predict the performance of rotors with rectangular and tapered blades. Figure 23 shows the model and the experimental results for all the airfoil cambers studied. Relative proportions of the curves and overall magnitudes are captured by the model; however, clear differences with the experimental values are present. These are more evident when looking at the representative case shown in Fig. 24, where $C_T$ vs FM and $C_T$ vs $C_P$ are shown. For most collectives, $C_T$ predictions were satisfactory, except at 18 deg, where the model predicts a sharp drop in thrust. The model tends to overpredict FM at the lower angles of attack, and, for $C_T$, a sharp stall is present at 18 deg. The $C_T$ vs $C_P$ plot shown in Fig. 24 and the calculated spanwise distribution of induced angle of attack at the various collectives shown in Fig. 25 are useful to visualize the issues.

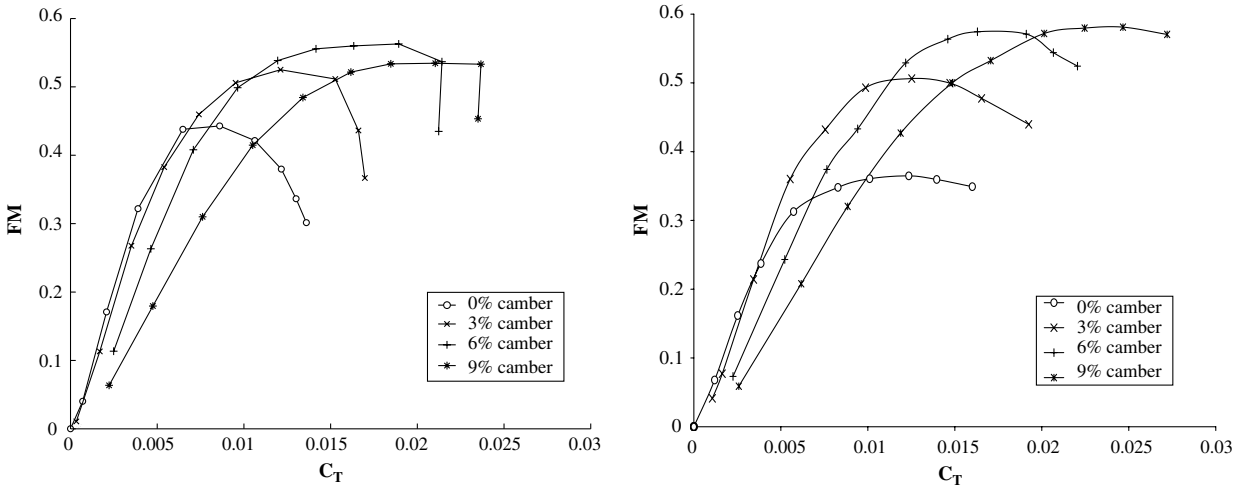


**Fig. 23 Predicted and experimental $C_T$ vs FM for 0, 3, 6, and 9% camber airfoils at 2500 rpm.**

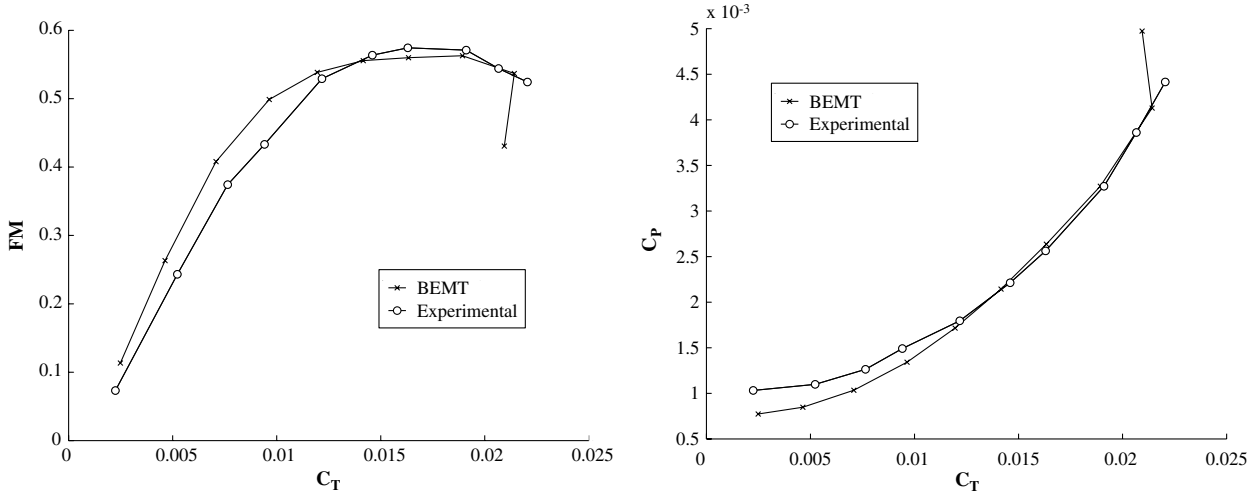


**Fig. 24 Predicted and experimental $C_T$ vs FM and $C_T$ vs $C_P$ for rotors with 6% camber airfoils at 2500 rpm.**

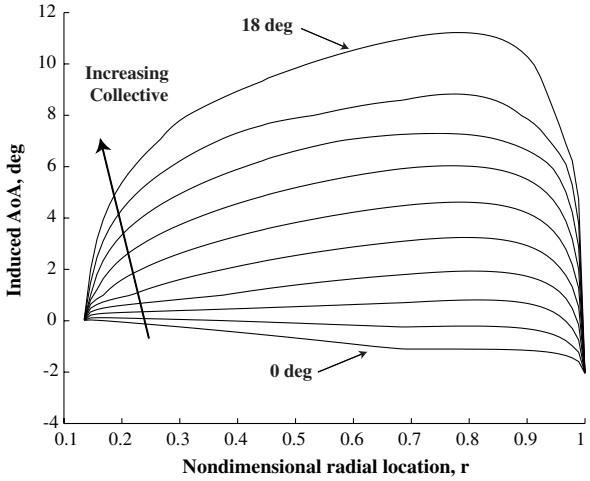


**Fig. 25 Induced angles of attack (AoA) at various collectives from BEMT for the 6% camber MAV rectangular blades at 2500 rpm.**

At low collectives, where the lower angles of attack occur, the computed $C_P$ is below the measured values; this is consistent with the inaccuracies in the calculation of the aerodynamic coefficients with CFD (Fig. 22). At higher collectives there is a region where the best agreement between predicted and measured values is achieved; however, the inability of the CFD to follow lift results in an early stall in the model calculations.

Similar results were obtained with the tapered blades. The model captured the main experimentally observed effect of taper: increased maximum FM and reduction in achieved thrust coefficients. As for the rectangular blades, quantitative errors in the magnitude of the FM curve were present. However, in this case, maximum FM predictions were below the experimental ones. Figure 26a shows the model and experimental results for a set of representative rectangular and tapered blades at 3000 rpm. Figure 26a shows the percentile error of FM predictions vs $C_T$.

Based on the previous comparisons, the direct use of the CFD database introduces errors in the blade lift predictions over the regions with high angles of attack and in the drag values over the regions with low angles of attack. Despite these issues, a qualitative agreement between experimental and numerical results allows the trends that can be used to improve rotors within the design space to be identified. To enhance the predictive capabilities of the model, the airfoil database needs to be refined. Results obtained with an enhanced database are discussed in the following section.

### B. Nano-Air-Vehicle-Scale Results: Refined Database

Achieving better rotor performance predictions requires the application of the empirical corrections proposed in Sec. V.A to the CFD-calculated database. The CFD results are used as an initial guess to the algorithm in Fig. 19, and the experimental data measured with the NAV-scale rotors are used as ground truth data in the refinement process of the respective database regions ($5 < Re < 20$ k). Experimental NAV-scale data and the CFD-calculated database share similar discretization in camber and $Re$, simplifying the overall process by avoiding additional rotor testing.

Figure 27 shows a representative case comparing the original CFD-calculated and empirically corrected lift and drag coefficients of a 4.5% camber airfoil. At a $Re$ of 10,000, the shape of the $C_l$ vs $\alpha$ curve is quite different than that used in the CFD validation at a $Re$ of

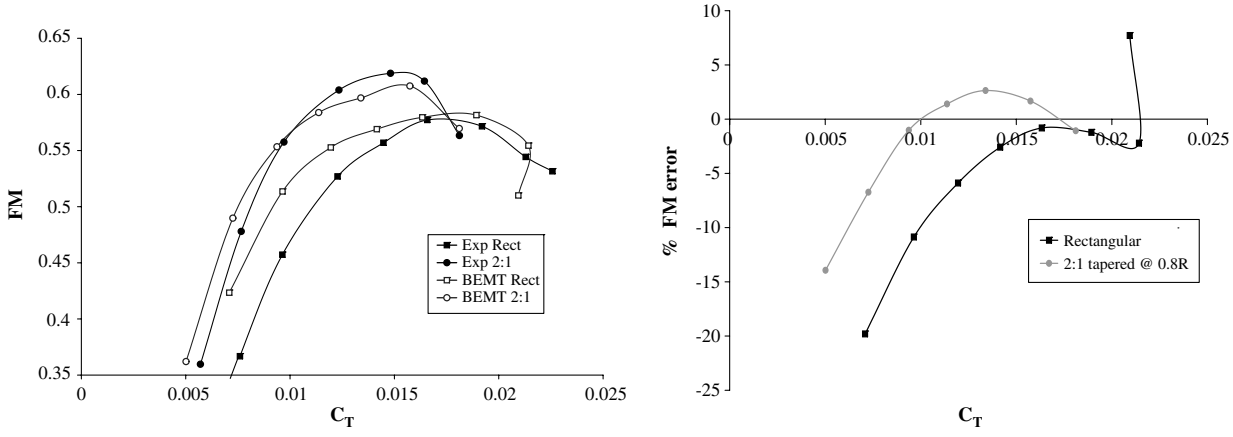


**a) Predicted and experimental $C_T$ vs. FM** **b) % FM error vs. $C_T$**

**Fig. 26 Predicted and experimental $C_T$ vs FM for rotors with rectangular and 2:1 tapered blades with 6% baseline camber at 3000 rpm, and % FM error vs $C_T$.**

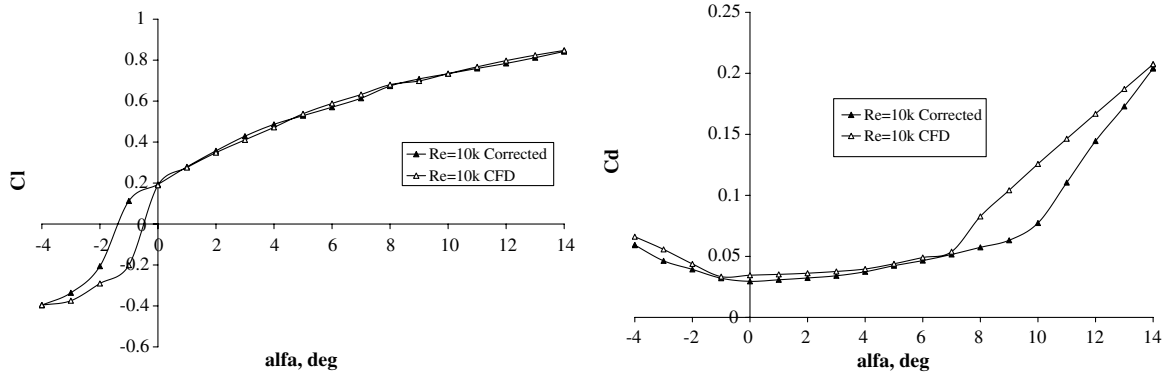


**a) Lift coefficient** **b) Drag coefficient**

**Fig. 27 CFD-calculated and empirically corrected aerodynamic coefficients for a 4.5% camber circular arc at $Re = 10$ k.**

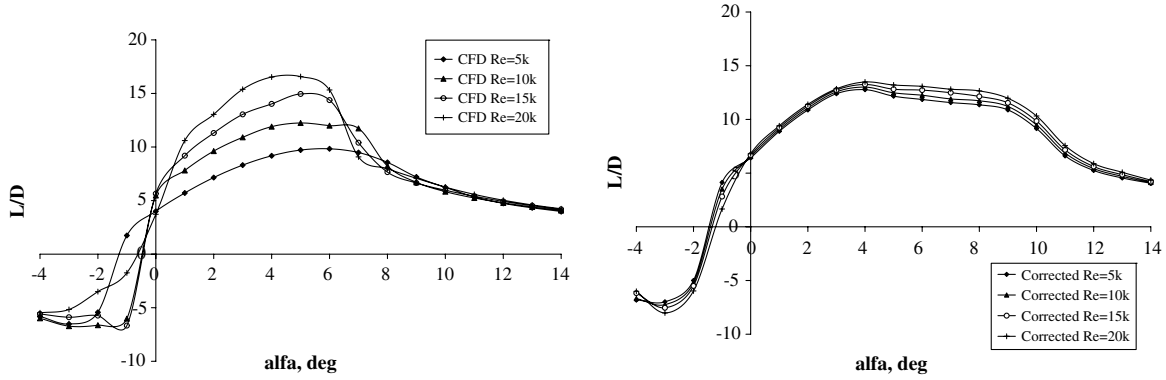


**a) CL/CD from CFD** **b) CL/CD after empirical corrections**

**Fig. 28 $L/D$ at various $Re$ before and after empirical corrections were applied on a 4.5% camber circular arc.**

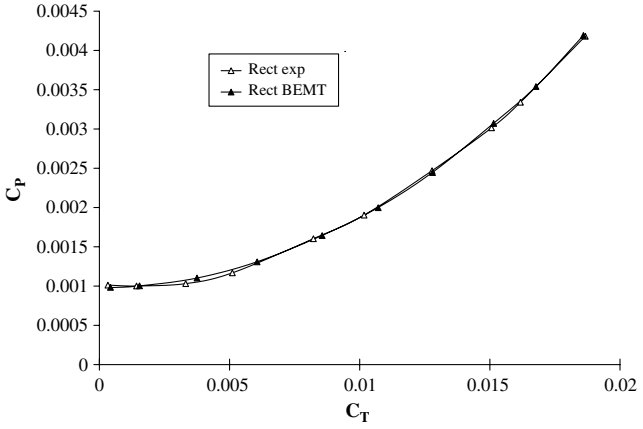


**Fig. 29 Predicted and experimental $C_T$ vs $C_P$ for rectangular bladed rotor with 4.5% camber at 10000 rpm.**

60,000. For the lower $Re$ cases, there is no lift stall in the range of angles of attack covered. However, as in the validation case, there is a clear drag stall.

Empirical corrections to the lift coefficient curve were relatively minor, mainly affecting the zero-lift angle of attack. On the other hand, the drag corrections were more pronounced, reducing the drag coefficient values at low angles of attack and delaying stall by about 4 deg. The corrections in lift and drag had a noticeable effect in the $L/D$ ratio of the airfoil over the $Re$ range considered. Figure 28 compares the $L/D$ ratio before and after the adjustments. The relative magnitude and overall curve shapes were modified, lowering the maximum $L/D$. The rectified curves exhibit an almost uniform shape and magnitude, showing that $Re$ effects are much more subtle than what CFD predicts.

Figure 29 shows the predicted and the measured $C_T$ vs $C_P$ plots for the sample rotor case using the refined database. The overall curve shapes are almost perfectly matched; however, offsets in the collectives are present. The exact collective pitch at which the measurements are taken have a slight degree of uncertainty because it is likely that small blade deflections occur during operation. This is particularly true for NAV rotor experiments, considering that the stiffness of the material used to manufacture the blades is relatively low. To obtain smooth $C_l$ and $C_d$ vs $\alpha$ curves, the algorithm tries to match the curve shapes giving some flexibility on the collective at which experimental $C_T$ and $C_P$ values are reached. If this is not done, even the smallest experimental error would result in jagged aerodynamic coefficient curves.

The refined database was used to predict the performance of NAV rotors with a 2:1 taper ratio starting at 80% of the span using a baseline camber of 4.5%. Experimental and model $C_T$ vs FM plots using rectangular and tapered blades are shown in Fig. 30a. The effect of tapering the blades is clearly reflected in the predictions that show the curve shifting to the right and undergoing an increase in maximum FM. The error in FM predictions, shown in Fig. 30b, is smaller than for the MAV-scale rotors of Fig. 26b. However, even with the refined database, maximum FM is still underpredicted by about 2.5%. This result makes the limitation of the model that calculates the rotor inflow by factoring the blade and airfoil geometries through interpolation of the preexisting airfoil database evident. Higher-order effects resulting from the blade tip shape and planform can introduce changes in the wake structure that affect the rotor performance. As mentioned earlier, the model implementation currently uses Prandtl's tip loss function to model tip losses [13], which is a function of the number of blades and induced inflow angle.

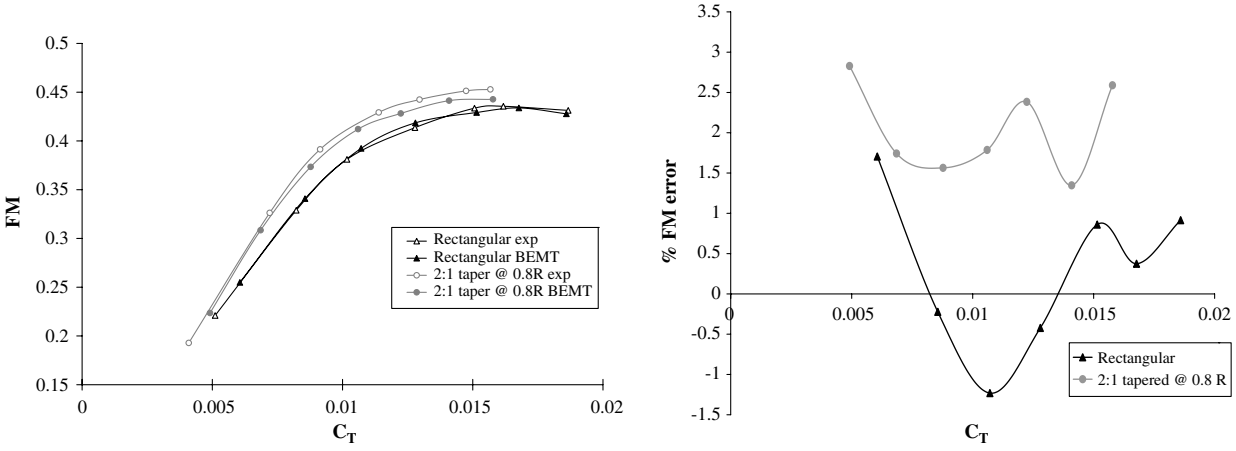


**a) Predicted and experimental $C_T$ vs. FM** **b) % FM error vs. $C_T$**

**Fig. 30 Predicted and experimental $C_T$ vs FM for rectangular and tapered rotors with 4.5% baseline camber at 10000 rpm, and percent FM error vs $C_T$.**

**Table 4 Optimization parameters, ranges, and results for NAV rotor case study**

| Parameter | Range | Optimized value |
|---|---|---|
| Camber at root | 4.5–7.5% | 6% |
| Camber at tip | 4.5–7.5% | 7.50% |
| Radial cut, pt. 5 (see Fig. 4) | 0.5–0.8$r$ | 0.65$r$ |
| Chordwise cut, pt. 4 (see Fig. 4) | $-c/2$ $c/4$ | 0 |
| Twist root angle | 0–5 deg | 3.5 deg |
| Twist angle at control point (see Fig. 5) | 0–3 deg | 0.5 deg |
| Twist angle at blade tip (see Fig. 5) | 0.5–0.7$r$ | 0.6$r$ |

Nevertheless, the errors introduced by the uncertainty in the aerodynamic coefficients were greatly reduced with the empirical corrections on the airfoil data, allowing the use of the model as a more accurate design tool.

### C. Rotor Optimization Case Study

The optimization algorithm of Fig. 20 was used to find the best performing rotor within a defined design space. The objective was to design a 6 g helicopter with a 7.5 cm rotor diameter spinning at 7500 rpm. Baseline chord and root cutout were fixed at 1 cm and $0.35R$, respectively, and only asymmetric tapering at the trailing edge was allowed. Following the geometrical definition of Sec. VII.A, a total of seven variables were used in the optimization of the blade geometry. The model predicted an optimized rotor operating at a collective of 14.8 deg with a FM of 0.44 at the design point. Table 4 summarizes the design variables, the ranges considered, and the optimization results. Figure 31 shows the resulting spanwise distribution of chord, camber, twist, and $Re$ along the optimized blade.

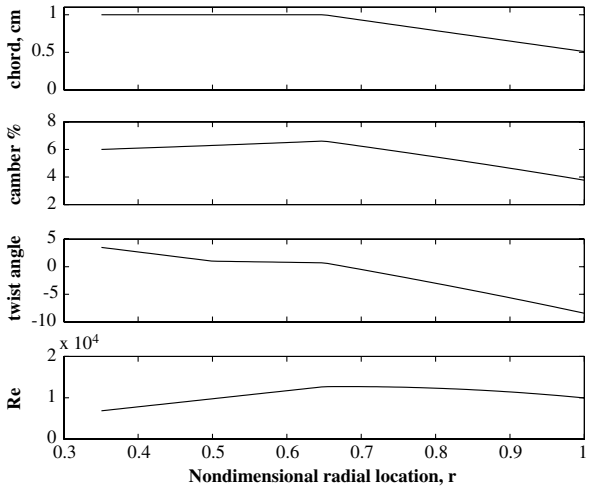


**Fig. 31 Geometric and operating characteristics along blade span of optimized geometry.**

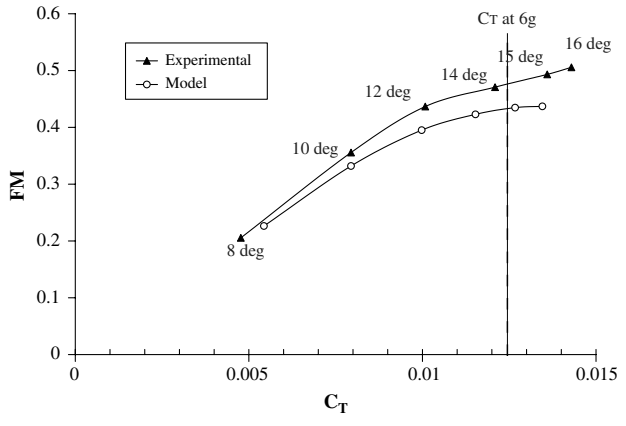


**Fig. 32 Experimental performance of optimized NAV rotor.**

The rotor was manufactured following the same rapid prototyping technique used in the hover NAV-scale experiments and was tested over a range of collectives. Figure 32 compares the predicted and experimental performance in terms of FM. For this particular case, rotational speed and rotor diameter were fixed, hence there was no difference between the use of FM or PL as efficiency metric in the optimization process. The 6 gf of required thrust were measured at a collective of 14.3 deg with a FM of approximately 0.47. The model underpredicted rotor efficiency at the design point in terms of FM by 3 percentage points at a collective 0.6 deg higher. As for the validation case of Fig. 30a, it is possible that aerodynamic forces introduce blade deflections and that unsteady aerodynamic phenomena with a positive effect on rotor performance are present at the higher thrust levels. Both of these factors are unaccounted for in the model and may be linked to the errors in performance predictions. The robustness of the optimization was tested by deviating from the optimized rotor geometry. A few rotors with various taper start locations were experimentally tested, resulting in lower performance levels at the required thrust, giving confidence to the validity of the approach presented in this paper.

## VIII. Conclusions

The final result of this investigation is the development of a low computational cost approach to design and optimize MAV and NAV rotors for hover over a wide range of $Re$, thrust, and power requirements. The design space was limited to Reynolds numbers between 5000 and 60,000 and to the use of a specific family of circular arc airfoils. The choice of circular arcs in the current investigation was based on results of previous research that identified the following positive aerodynamic characteristics over the Reynolds number range covered: 1) higher maximum lift coefficients than conventional airfoils, 2) lower minimum drag coefficients than conventional airfoils, 3) low dependency of lift and drag coefficients with Reynolds number, 4) low dependency of lift coefficient slope with Reynolds number, 5) minimal hysteresis loops when cycling Reynolds numbers or angle of attack, and 6) low sensitivity to ambient turbulence.

A blade parameterization that couples blade planform, camber, and twist distributions was developed and used to systematically define blade shapes that are easily manufactured and that include key geometric elements that can produce an efficient hovering rotor design. The blade–airfoil parametric definition was incorporated into a BEMT model coupled to an airfoil database. The algorithm interpolates the database to obtain the lift and drag coefficients at each blade element, which are then used to calculate the rotor inflow through an iterative process. Interpolation is performed in three dimensions: camber, $Re$, and angle of attack.

The proposed approach requires the airfoil database used for interpolation to be obtained. During the course of this investigation, two different methods were used for generation of the database. One was purely numeric in nature, using the incompressible two-dimensional CFD solver INS2D to calculate the aerodynamic coefficients. The second used the rotor performance data of rectangular bladed rotors over a range of rotational speeds, cambers, and angles of attack to obtain the lift and drag coefficients using a reverse BEMT algorithm.

Validation of the model with the experimental data acquired at MAV scale using the CFD-calculated database showed that, for the most part, thrust predictions were satisfactory. Although performance predictions were generally higher than the experimental values, due to an underprediction of the drag coefficients, the main trends in performance resulting from blade geometry and rotor operating conditions were captured by the model.

The quantitative errors resulting from the CFD-generated database limited the use of the model to first-order rotor sizing. The empirically corrected database produced a set of lift an drag coefficients that are consistent with the airfoil geometries tested and that factor higher-order effects such as geometric imperfections, surface finish, and aerodynamic unsteady phenomena not addressed

in the CFD study performed. These refinements resulted in an improvement of the overall model predictive capabilities.

The broad range of possible configurations in the MAV and NAV vehicle scales requires the use of an unambiguous efficiency metric in the design process. Whereas FM is generally used in full-scale rotor design, PL is a better choice when rotational speed, rotor diameter, and disk loading are design variables. The optimization scheme implemented uses PL as its main criteria to determine the best performing rotor in the design process.

The methodology proposed requires an initial investment of computational and experimental efforts to calculate the comprehensive database that includes all desired airfoils at the various angles of attack and $Re$, however, this is only required once. After the database has been calculated and validated, the only computational cost for each design case involves running the BEMT algorithm. The low computational cost of the BEMT model makes the use of an optimization scheme practical. With the proposed approach, a typical desktop computer can be used to perform a representative optimization, where a grid search of about 5000 cases takes mere hours. This is only a fraction of the time required for a single three-dimensional CFD case to run using much broader computational resources. Additionally, due to the fact that several of the higher-order aerodynamic effects are factored in the empirically corrected coefficients, predictions have a generally good agreement with the actual rotor performance, which is still challenging to systematically achieve in three-dimensional CFD simulations.

## References


[1] Zdunich, P., Bilyk, D., MacMaster, M., Loewen, D., DeLaurier, J., Kornbluh, R., Low, T., Stanford, S., and Holeman, D., "Development and Testing of the Mentor Flapping-Wing Micro Air Vehicle," *Journal of Aircraft*, Vol. 44, No. 5, 2007, pp. 1701–1711. doi:10.2514/1.28463

[2] Sirohi, J., Tishchenko, M., and Chopra, I., "Design and Testing of a Micro-Aerial Vehicle with a Single Rotor and Turning Vanes," *Proceedings of the AHS 61th Annual Forum* [CD-ROM], American Helicopter Society, Alexandria, VA, June 2004.

[3] Lipera, L., Colbourne, J. D., Tishcler, M. B., Mansur, M. H., Rotkowitz, M. C., and Patangui, P., "The Micro Craft iSTAR Micro Air Vehicle: Control System Design and Testing," *Proceedings of the AHS 57th Annual Forum*, [CD-ROM] American Helicopter Society, Alexandria, VA, June 2001.

[4] Bohorquez, F., Samuel, P., Sirohi, J., Pines, D., Rudd, L., and Perel, R., "Design Analysis and Hover Performance of a Rotary Wing Micro Air Vehicle," *Journal of the American Helicopter Society*, Vol. 48, No. 2, April 2003, p. 80.

[5] Hein, B. R., and Chopra, I., "Hover Performance of a Micor Air Vehicle: Rotors at Low Reynolds Number," *Journal of the American Helicopter Society*, Vol. 52, No. 3, July 2007, pp. 254–262. doi:10.4050/JAHS.52.254

[6] Pines, D., and Bohorquez, F., "Challenges Facing Future Micro-Air-Vehicle Development," *Journal of Aircraft*, Vol. 43, No. 2, March–April 2006, pp. 290–305. doi:10.2514/1.4922

[7] Bohorquez, F., and Pines, D., "Hover Performance and Swashplate Design of a Coaxial Rotary Wing Micro Air Vehicle," *Proceedings of the AHS 60th Forum* [CD-ROM], American Helicopter Society, Alexandria, VA, June 2004.

[8] Carmichael, B. H., "Low Reynolds Number Airfoil Survey," Vol. 1, NASA CR 165803, Nov. 1981.

[9] Kroo, I., and Kunz, P., "Meso-Scale Flight and Miniature Rotorcraft Development," *Fixed and Flapping Wing Aerodynamics for Micro Air Vehicle Applications*, edited by T. J. Mueller, Progress in Astronautics and Aeronautics, AIAA, Reston, VA, 2001, pp. 503517.

[10] Schmitz, F. W., *Aerodynamik des Flugmodells*, C. J. E. Volkmann Nachfolger E. Wette, Berlin, 1942; also "Aerodynamics of the Model Airplane, Part I: Airfoil Measurements," Redstone Scientific Information Center, N70-39001, RSIC-721, Redstone Arsenal, Nov. 1967 (in English).

[11] Laitone, E. V., "Aerodynamic Lift at Reynolds Numbers Below 70,000," *AIAA Journal*, Vol. 34, No. 9, 1996, pp. 1941–1942. doi:10.2514/3.13329

[12] Mueller, T. J., "Aerodynamic Measurements at Low Reynolds Numbers for Fixed Wing Micro-Air Vehicles," *RTO AVT Course on Development and Operation of UAVs for Military and Civil Applications*, von Karman Inst. for Fluid Dynamics, Rhode-Saint-Genese, Belgium, Sept. 1999.

[13] Leishman, J. G., *Principles of Helicopters Aerodynamics*, Cambridge Univ. Press, New York, 2000.

[14] Bohorquez, F., "Rotor Hover Performance and System Design of an Efficient Coaxial Rotary Wing Micro Air Vehicle," Ph.D. Dissertation, Aerospace Engineering Dept., Univ. of Maryland, College Park, MD, 2007.

[15] Rogers, S. E., and Kwak, D., "An Upwind Differencing Scheme for the Steady-State Incompressible Navier–Stokes Equations," NASA TM 101051, Nov. 1988.

[16] Rogers, S. E., and Kwak, D., "An Upwind Differencing Scheme for the Time Accurate Incompressible Navier–Stokes Equations," *AIAA Journal*, Vol. 28, No. 2, 1990, pp. 253–262. doi:10.2514/3.10382

[17] Kunz, P. J., "Aerodynamics and Design for Ultra-Low Reynolds Number Flight," Ph.D. Dissertation, Dept. of Aeronautics and Astronautics, Stanford Univ., Palo Alto, CA, June 2003.

[18] Kroo, I., and Kunz, P., "Analysis and Design of Airfoils for Use at Ultra-Low Reynolds Numbers," *Fixed and Flapping Wing Aerodynamics for Micro Air Vehicle Applications*, edited by T. J. Mueller, Progress in Astronautics and Aeronautics, AIAA, Reston, VA, 2001, p. 503517.

[19] Schroeder, E., and Baeder, J., "Using Computational Fluid Dynamics for Micro Air Vehicle Airfoil Validation and Prediction," AIAA Paper 2005-4841, 2005.

[20] Schroeder, E., "Low Reynolds Number Flow Validation Using Computational Fluid Dynamics with Applications to Micro Air Vehicles," M.S. Thesis, Dept. of Aerospace Engineering, Univ. of Maryland, College Park, MD, 2005.

[21] Lakshminarayan, V., Bush, B., Duraisamy, K., and Baeder, J., "Computational Investigation of Micro Hovering Rotor Aerodynamics," AIAA Paper 2006-2819, 2006.

[22] Spalart, P., and Allmaras, S., "A One Equation Turbulence Model for Aerodynamic Flows," AIAA Paper 92-0439, 1992.

[23] Gad-El-Hak, M., *Flow Control: Passive, Active, And Reactive Flow Management*, Cambridge Univ. Press, Cambridge, England, U.K., 2000.

[24] Barber, T. J., "An Investigation of Strut-Wall Intersection Losses," *Journal of Aircraft*, Vol. 15, No. 10, 1978, pp. 676–681. doi:10.2514/3.58427

[25] Mueller, T. J., Jansen, B. J., Jr., "Aerodynamic Measurements at Low Reynolds Numbers," AIAA Paper 82-0598, March 1982.

[26] Spalart, P. R., "Trends in Turbulence Treatments," AIAA Paper 00-2306, July 2000.